CHARACTERIZATION OF CONTACT MECHANISMS AND EFFECT OF ELECTRON IRRADIATION IN CARBON NANOTUBE FIELD EFFECT TRANSISTORS

by

David Perello

BS, Electrical Engineering, University of Pittsburgh, 2007

Submitted to the Graduate Faculty of

The Swanson School of Engineering in partial fulfillment

of the requirements for the degree of

Master of Science

University of Pittsburgh

2010

UNIVERSITY OF PITTSBURGH

SWANSON SCHOOL OF ENGINEERING

This thesis was presented

by

David Perello

It was defended on

August 10th, 2009

and approved by

Dr. Guangyong Li, Assistant Professor, Department of Electrical and Computer Engineering

Dr. Mahmoud El Nokali, Professor, Department of Electrical and Computer Engineering

Dr. Young Hee Lee, Professor, Department of Physics, Sungkyunkwan University, Suwon Republic of Korea

Thesis Advisor: Dr. Minhee Yun, Assistant Professor, Department of Electrical and Computer Engineering

CHARACTERIZATION OF CONTACT MECHANISMS AND EFFECT OF ELECTRON IRRADIATION IN CARBON NANOTUBE FIELD EFFECT TRANSISTORS

David Perello, M.S.

University of Pittsburgh, 2010

We have fabricated electrical devices based on thermal chemical vapor deposition (TCVD) grown single walled carbon nanotubes (SWCNTs). Long SWCNT are utilized to analyze electrical transport properties and extract contact data including Schottky Barrier heights (SBHs) and contact resistance. For all studies performed, multiple contact metals were used, and tens to hundreds of devices were fabricated on single CNT. This mass production method allows comparison of results, as well as greater options in device analysis.

To analyze SBHs at carbon nanotube – metal contacts, field effect transistor (FET) devices were examined using AFM, low temperature measurements in closed – cycle refrigerator (CCR), and electrical characterization. SBH is measured on carbon nanotubes with multiple metal contacts for comparison purposes, with barriers extracted via low temperature activation energy measurements and nonlinear curve fitting using the program Origin. Two methods were utilized in the fabrication of carbon nanotube devices for the SB study. The first incorporated both electron beam lithography (EBL) for exposures and focused ion beam (FIB) for deposition of lead lines between CNT contacts and large probe pads. The second method used only EBL to prevent the ionic exposure common in FIB.

The effect of using EBL with devices incorporating CNT has also been investigated. The effect on metallic and semiconducting CNT exposure in the channel of the transistor devices was

examined and a physical mechanism for the variations discussed. We show that the subsequent generation of trap states along the CNT channel varies the conduction mechanism of the nanotube and has a significant effect on device performance. Metallic and Semiconducting CNT react very differently, with an apparent increased localization in the metallic tubes responsible for dramatic decreases in conductance.

TABLE OF CONTENTS

LIST OF TABLES

LIST OF FIGURES

PREFACE

I would like to thank my advisor, Dr. Minhee Yun, for giving me the opportunity, guidance, and support for me to succeed on the work in this thesis and other endeavors. I am grateful not only for this, but his persistent guidance and goal of improving my succcess as a research scientist in the future.

Secondly I would like to thank Dr. Young Hee Lee at Sungkyunkwan University for serving as a secondary advisor for the carbon nanotube work. His knowledge of carbon nanotubes and guidance in his lab during my summer trips to korea have made this work possible and enjoyable.

I also want to thank Professor Mouhmad El Nokali and Assistant professor Guangyong Li for joining my thesis committee, and for their help throughout the years in various classes and important academic matters.

Last, but not least, I would like to thank my family for their love and support, as well as my fellow researchers Innam Lee, Yushi Hu, Michael Nayhouse, Dr. Hoil Park, Dr. Seong Yol Jeong, Dr. Dong Jae Bae, and Woojong Yu for their support, wisdom, and contributions to my learning and growth through the past few years. Research is never an independent matter, and their thoughts, help, and friendship were instrumental in my work.

1.0 INTRODUCTION

1.1 MOTIVATION

Nearly two decades after their accidental discovery, CNT have remained one of the hottest topics in nanoelectronics research. CNT structure is that of a cylindrically wrapped hexagonal aligned sheet of carbon atoms (called graphene). Species of CNT with a single cylinder of carbon atoms are denoted single walled and have diameters ranging from 4 Å to around 2.5 nm. Multiwalled CNT (MWCNT) are nanotubes with more than one wall of carbon atoms wrapped around in concentric circles. Diameters of MWCNT can range from ~ 2 - 100 nm, and have between two and a few tens of concentric carbon walls.

One reason CNT have remained such a hot topic due to their resistance to a number of common phenomena that plague monolithic semiconducting device performance. Firstly, due to the single – crystal nature and strong Sp_2 bond strength of the carbon atoms, diffusion of carbon atoms is impossible. The lattice structure of CNT is composed of hexagonal honeycomb arrangement of carbon atoms bonded by Sp^2 hybridized covalent bonds. Without defects, this arrangement generates a structure with a Young's modulus and tensile strength of CNTs estimated via molecular dynamics simulations to be greater than 1 TPa [1]. The ideal values for these quantities match or exceed the best commercially available materials on the market, Indicating CNT may be incorporated into future materials to tailor material properties.

The lattice structure, Brillouin zone and unit cell of CNT are defined in terms of graphene. Figure 1.1 details the graphene honeycomb lattice with the reciprocal space vectors a_1 and a_2 defined. A graphene unit cell contains two atoms at the locations (in terms of a_1 and a_2) $\frac{1}{3}(a_1 + a_2)$ and $\frac{2}{3}(a_1 + a_2)$. These basis vectors are further used to define the structure of a SWCNT. SWCNT are classified and identified by interpreting the cylinder as a sheet of graphene wrapped via the chiral vector. This chiral wrapping vector is defined as:

$$c = na_1 + ma_2 \tag{1.1}$$

Where n, m defines the chiral indices of the nanotube, and will become useful later when electrical properties are defined in terms of these values. The wrapping angle or chiral angle of a CNT is defined as:

$$\cos(\theta) = \frac{(n_1 + n_2)}{2\sqrt{n_1^2 + n_1 n_2 + n_2^2}} \tag{1.2}$$

The chiral angle is the angle between the basic vector a_1 and the chiral vector c. Figure 1.1 can be seen for the graphical interpretation of this value. As can be inferred from the definition of the chiral vector, the diameter of a SWCNT is simply the length of c:

$$d = \frac{|c|}{\pi} = \frac{|a_1|}{\pi}\sqrt{n_1^2 + n_1 n_2 + n_2^2} = \frac{a_0}{\pi}\sqrt{n_1^2 + n_1 n_2 + n_2^2} \tag{1.3}$$

Where $a_0 = |a_1| = |a_2|$. Later, when discussing electronic band structure, these quantities based upon the chiral indices will be utilized in defining quantization conditions and other values. further subcategories of carbon nanotubes are hence defined based on the indices, with

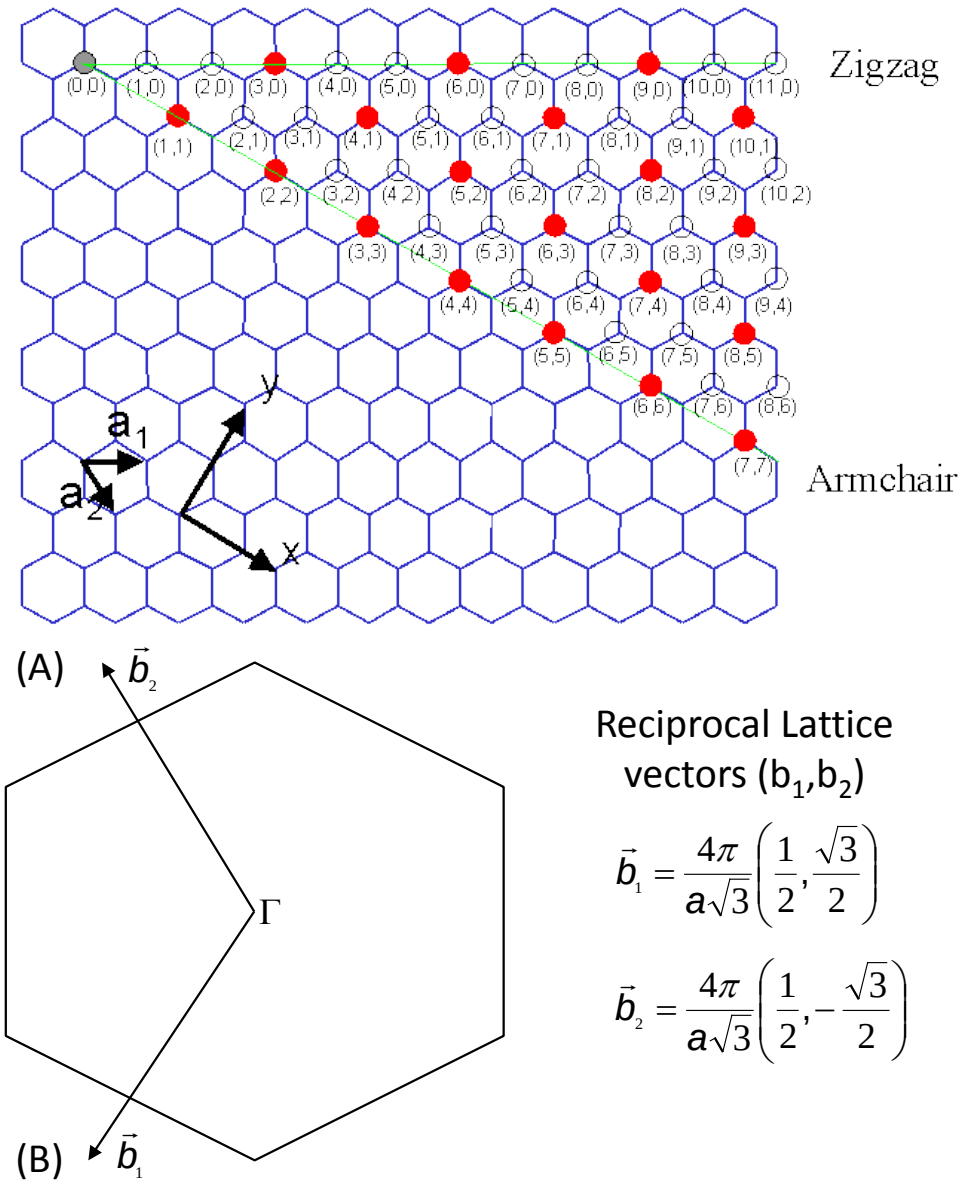

Figure 1.1 (A) Diagram of graphene with chiral vector and wrapping angle used to constructure CNT from graphene lattice [2]. (B) Graphene Brillouin zone with corresponding reciprocal lattice vectors defined.

each having unique characteristics: SWCNT are further divisible into three classifications dependent upon these chiral indices: armchair, chiral, and zigzag. Armchair tubes are those

SWCNT with an index of (n,n) and are unique by their metallic character. Chiral CNT are those having indices (n,m) and may have either metallic or semiconducting character. They are further defined by (in most cases) a very large unit cell. Lastly, zigzag SWCNT denote those with (n,0) index and may be either semiconducting or metallic dependent upon the value of n.

Electronically, carbon nanotubes can be semiconducting or metallic as determined by the chiral vector and chiral indices. The simplest method for deriving the band structure of SWCNT is nearest-neighbor tight binding calculations for graphene and applying the zone folding (confinement) approximation. See Appendix B for full derivation of the graphene band structure. Before application of the confinement approximation, the band structure of graphene has the form:

$$E^{\pm}(k_1,k_2)=\frac{\varepsilon_{2p}\pm\gamma_0\sqrt{3+2\cos 2\pi k_1+2\cos 2\pi k_2+2\cos 2\pi(k_1-k_2)}}{1\pm s_0\sqrt{3+2\cos 2\pi k_1+2\cos 2\pi k_2+2\cos 2\pi(k_1-k_2)}} \qquad (1.4)$$

Where $\varepsilon_{2p},\gamma_0,s_0$ are the self interaction energy of individual carbon atom (and is zero in the simplified model), the carbon-carbon interaction energy, and overlap integral (see appendix B). By matching with ab initio calculations, we can estimate the semi – empirical constants γ_0 = -2.84 eV and s_0 = .07. To find the band structure of SWCNT, we must add a confinement or zone-folding approximation. Along the length of the CNT, the tube is usually assumed to be semi-infinite and thus there exists a continuous wave vector in this direction. Along the circumference (parallel to chiral vector c) any wave vector $k_\perp$ is quantized by the condition:

$$k\cdot c=2\pi m \qquad (1.5)$$

Where c is the chiral vector and m is an integer. Only those k that satisfy the above equation are allowed electronic states. This results in a set of discrete allowable energy bands – composing the band structure of a SWCNT. Figure 1.2 shows the resulting discrete energy levels, and shows the match of nearest neighbor tight binding with zone folding when compared to a much more complex ab initio calculation.

The discrete allowable states crossing the graphene Brillouin zone also determine whether the CNT is metallic or semiconducting. If an energy bands crosses one of the 6 zero – gap graphene k – points, the CNT will be metallic in nature. This condition is satisfied if:

$$k \cdot c = 2\pi m = \frac{2\pi}{3}(n_1 - n_2) \tag{1.6}$$

This can further be simplified to the condition:

$$3m = n_1 - n_2 \tag{1.7}$$

'm' is once again a positive integer [3,4]. Equation 1.7 tells us that if the difference in the chiral indices is a multiple of 3, the nanotube will be metallic. Uniquely, these considerations allow a tailorable electronic band structure through the production of CNT with various chirality and diameters. It also induces some very interesting 1 – dimensional effects on the density of states (DOS). Due to the low dimensionality of CNT, the min and max of the energies bands (for metallic or semiconducting) are parabolic in nature. In i one – dimensional conducting channels, the DOS is given by [5]:

$$n(E) = \frac{2}{q|k_z|}\sum_i dk_z \delta(k_z - k_i)\left|\frac{\partial E^{\pm}(k_{\perp}, k_z)}{\partial k_z}\right|^{-1} \tag{1.8}$$

Following the derivation by Mintmire and White in 1998 [5] this results in a final DOS of the form:

$$n(E) = \begin{cases} B \sum_{m=-\infty}^{\infty} \frac{|E|}{\sqrt{E^2 - E_m^2}} & |E| > |E_m| \\ 0 & |E| < |E_m| \end{cases} \qquad (1.9)$$

B is a constant dependent upon the diameter, overlap integral, and carbon – carbon equilibrium distance. As could be expected in a one – dimensional structure, a series of Van Hove singularities (VHS) are induced at the band edges [6]. Also interesting in this approximation by Mintmire and White is the lack of chirality dependence. The diameter is the only factor that determines the bandgap, yielding some inaccuracies on the order of tens of meV due to the non-circular symmetry of the energy bands with respect to the center of a graphene Brillouin zone. Moving away from the k points, spherical energy contours become more triangular – requiring correction factors to improve correlation between ab initio and zone-folding methods [3]. Trigonal warping is the root cause of these deviations in the energy bands and is well documented theoretically and experimentally [7,8].

The existence of VHS in CNT allows for important optical identification of specific chirality and diameter via Resonant Raman Scattering and spectrofluorimetric measurements [9-12]. If incident radiation is in resonance with the energy gap between two VHS, enhanced emission occurs that enables identification of specific nanotube species and diameter [11]. Work in this area is well documented, and nanotubes may be identified via matching the excitation energy with the Raman shift – and then consulting the so – called Kataura plot [13] to match the exact chirality.

SWCNTs unique quasi 1-D electronic structure allows it to be incorporated into devices to demonstrate and study a plethora of fundamental phenomena such as Lüttinger liquid behavior, Coulomb blockade, spin-orbit coupling, ballistic electron transport [14-16], Aharanov – Bohm oscillations [17], and conductance quantization [18]. Due to the purity of the CNT structure, defect scattering of electrons can be almost nonexistent for submicron critical dimensions [18,19].

Carriers injected into a nanotube channel via contacts are scattered elastically by high energy optical phonons for applied bias greater than ~15 meV [20-22]. Theoretical calculations estimate an optical phonon mean free path 10-30 nm [23]. Experimentally, devices fabricated at this length scale are capable of holding currents around 100 μA [24,25]. Typical devices are fabricated with much longer channel length, yet still are capable of carrying close to the ballistic conductance limit due to the micron length acoustic phonon scattering mean free path in pure SWCNTs [26].

The first transistor demonstration with a CNT acting as the semiconducting channel was done in 1998 by Tans *et al* [27] and by Martel *et al* [28]. Advances in the last 11 years have allowed fabrication of switching devices using CNT to produce some of the best transconductance, mobility, current density, On/Off ratio recorded in the literature – even compared with. These advances were in part due to the discovery of ohmic contacts to semiconducting devices with Pd [29,30], Rh [29], and Sc [16] metals resulting from the simple work function alignment of these metals with the CNT valence or conduction bands without high-temperature annealing processes. Other electrical devices fabricated include a Ring Oscillator [31,32] multiple carbon nanotubes, as well as another with 12 side – by – side FETs fabricated on a single SWCNT with excellent frequency response and 52 MHz operation [31,32]. SWCNT devices have also shown ambipolar transistor switching – a quality that previous n or p – doped semiconductors were incapable of having due to fixed majority carrier [33-35]. Although the physical and electronic properties of CNT warrant further study and exploration, there are many problems preventing commercialization. While nanotubes are grown

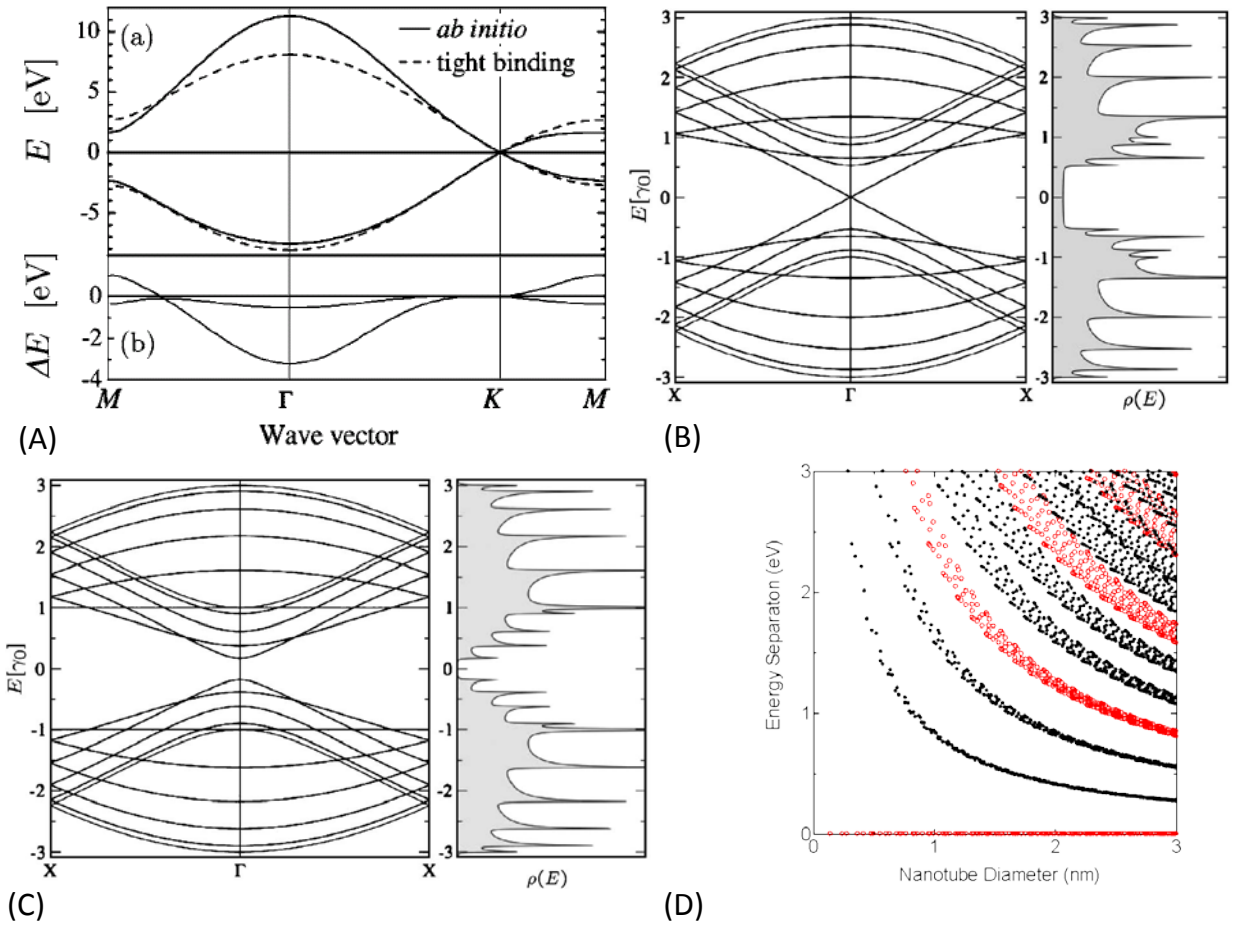

Figure 1.2 (A) Comparison of ab initio and nearest neighbor tight binding calculations – with empirical parameters estimated to best fit with the ab initio results [36]. (B) Energy bands and corresponding DOS of an (8,2) chiral CNT.[36] (C) Energy band diagram and DOS for (10,0) zigzag CNT [36]. (D) Kataura plot used to find CNT chirality by matching resonant Raman shift with energy gap between allowable transitions [2].

using a bottom-up approach, typically methods of incorporating the CNT into electrical devices utilize monolithic planar fabrication processes widely used in industry and academia. Many difficulties are generated via this conflict of process due to the differing temperature and placement opportunities for bottom up growth and planar fabrication. CNT device fabrication suffers from a number of problems generated from this conflict.

Firstly, growth processes for CNT often require large scale heating of the substrate in a chemical vapor deposition (CVD) furnace [37,37]. The heating of the silicon/oxide substrate to temperatures exceeding 900° Celsius in the presence of various gases leads to pinhole defects and leakage current in thin surface oxide layers. Therefore, lower temperatures, thicker oxides, or growth followed by pattern transfer have been utilized to reduce substrate leakage current. Other groups have further incorporated top-gate high – k dielectrics such as HfO_2 and Al_2O_3 for excellent transistor performance including transconductance and mobility [30,38]. This gate dielectric appears to have the effect of quenching soft-phonons, to further increase mobility in the nanotube when compared with bottom-gated layouts [30,38]. Further issues regarding the use of such fabrication methods will be mentioned in the later sections of this thesis.

Concentrating on CNT growth and not dispersion, precise control over the catalyst is also required so that only single or multi-walled CNT are produced during the high temperature growth processes. The catalysts act as seeds in the growth of the nanotubes, and must be placed very accurately to be included in monolithic process, unless use of solution dispersed nanotubes is implemented [39,40]. With solution dispersion, dielectrophoresis or other directional methods can be employed, although nanotubes utilized with this method have shown decreased performance [40]. Furthermore, direction remains a primary difficulty even with the great advances in aligned nanotube growth via laminar flow methods [41-43]. Yet, these methods cannot control the nanotube

diameter (and hence chirality) as well as the final length. Previous studies have indicated that very precise control of growth temperatures allows for constant diameter growth – although this method does not allow for specific (n,m) growth [44]. Defects in nanotubes can signify chirality changes, although this has been shown to happen over the course of many micrometers in high-purity tubes [45]. Since implemented device lengths (electrical, optical, and mechanical) are unlikely to reach longer than a few microns, the defect free length of a few millimeters is certainly acceptable. Growth methods thus far are unable to selectively generate metallic or semiconducting tubes, let alone specific chiral indices without post process treatment [46,47]. By definition, 2/3 of CNT are semiconducting by chirality, while the use of Plasma Enhanced CVD can induce greater than 90% semiconductor growth [48].

Lastly, post growth and placement – the contacts between metal electrodes and CNT have thus far been difficult to control. No comprehensive theory for contact resistance or SB height exists, and other parameters such as FET threshold voltage are largely uncontrollable. It is this topic that will be considered in this thesis, as well as consideration of the conduction mechanism and effects of electron irradiation via scanning electron microscope (SEM).

Before considering SB method analysis, first it is necessary to examine previous work in the area of contact and conduction mechanisms. The contact between metals and CNT has been studied previously [29,49-58]. Contact resistance was first studied in 1999 by Tersoff [50], who suggested that the fast decay of the electron wavefunction Fermi level states could induce a tunneling barrier at the contacts if a significant metal/CNT gap is present. The nature of the CNT wavefunction innately limits the strength of the coupling between metal and CNT due to quickly decaying behavior. Bachtold *et al* found that bombardment of the contact regions with electrons reduced contact resistance greatly [49].

The nature of the contact is found to be quite different than typical monolithic devices with fixed SBH from Fermi level pinning by the contact. The contacts behave as though the Fermi level is unpinned – possibly allowing one to manipulate device characteristics by choice of metal contacts [56]. This factor has been utilized to implement CNT based Schottky diodes using asymmetric work function metal contacts of Ti and Pt with high frequency applications in mind [59] as well as for simple demonstration [60]. Unpinned SBs also allow metal choice to align with valence or conduction band as described above – a process not possible in many standard semiconductor materials.

While the presence of an energy barrier is undisputed at the carbon nanotube metal interface, the nature of the conduction mechanism is difficult to analyze. Barrier heights are very difficult to extract due to the presence of a large tunneling current at the contact [61-63], forcing thermionic models to predict unnaturally low barrier heights. It has also been suggested that simple oxygen absorption at the contacts manipulates barrier properties and can limit tunneling, a factor that may be reflected in barrier measurements [63]. This fact is very difficult to experimentally prove, but oxidation of the metal at the contact can be prevented if the deposition is done in ultra high vacuum without any oxidative chemicals used in liftoff. Similarly, in other work, Ti was ohmically contacted to semiconducting tubes using a high temperature annealing process ~ 800° Celsius for formation of TiC [33]. These high-temperature anneals are not possible in industrial planar processes where performance reducing dopant diffusion and material coagulation will occur.

Therefore, for acceptance of CNT as a viable CMOS supplement (or alternative), the first step is to find consistent Schottky Barriers (SBs) between specific metals and CNT. Ohmic contacts are not required since SB FETs can be linked to form dopant – free logic circuits [16,64].

Efforts to estimate SB and contact effects will now be considered, after introducing relevant theories to applicable in CNT based devices.

1.2 THESIS ORGANIZATION

Chapter 2 introduces general background information of this thesis. General SBH concepts and an outline of thermionic emission theory is covered in the first section. The second section provides background information regarding hopping conductivity and the Poole Frenkel model.

Chapter 3 covers the measurement of SBHs using two different attempted methods. The first method incorporates EBL as well as FIB for the fabrication of CNT transistor devices. The second method uses only EBL for patterning, and emphasizes the resulting measurements of a Schottky diode CNT transistor. Benefits and difficulties of both methods are discussed.

Chapter 4 covers experimental studies of electrical transport characteristics in CNT irradiated with electrons using an EBL exposure method. The doses utilized are similar to that used in regular EBL patterning and shed light on the effect of fabrication process on device performance and transport mechanisms.

Chapter 5 concludes and summarizes the accomplishments achieved in these studies. Resulting publication of this work, as well as future endeavors and further research is discussed.

2.0 BACKGROUND

2.1 THERMIONIC EMISSION AT METAL – SEMICONDUCTOR INTERFACE

Originally proposed by Walter Schottky, SB is a measure of the difference between energy levels for the majority carrier crossing an MS interface. Schottky originally proposed that the energy mismatch is a function of the difference between the metal work function and semiconductor electron affinity. Variances in experimental data led to further additions including the concept of Fermi-level pinning (FLP). FLP conceptually is a measure of how independent SB height is to changes in metal work function – although more precisely other phenomenon such as dipole formation can be responsible for such independence. To further develop a theory that can be experimentally verified and fit with CNT experimental data, it should be noted that all SB theories can be separated into two categories: interacting and non – interacting. Here it is assumed that the CNT and metal contact are abrupt and non-interacting, for analysis purposes. Past work has attempted to include an interaction coefficient, although the physical interpretation of such relations is unclear [61]. Secondly, it will be assumed that the SBH is homogeneous – a fair assumption due to the extremely limited lateral dimensions of the interface. Thirdly, neglecting the contribution of tunneling and assuming only those electrons with enough thermal energy to surmount a barrier of undefined shape are capable of contributing to the conduction. This factor is the most controversial, and the results will show that tunneling is indeed a very significant

factor. Lastly, it should be noted that although this plays little role in the analysis – we do *not* need to assume limited amounts of scattering in the space-charge region near the interface. The validity of the thermionic model does not need to include this assumption, and resulting from vastly different scattering mechanisms in the channel and in the contacts, it is highly unlikely that electrons traversing the barrier from the metal have an identical velocity distribution as those carriers which have been optically scattered through the channel region travelling in the reverse direction across the barrier. Further, the CNT channel has a quasi – discrete DOS, therefore the carrier distribution is innately different then in a three dimensional structure. This argument is presented in detail by Tung[65] and other recent work [66,67].

Thermionic emission current from the metal to the semiconductor is described by the potential – independent relationship:

$$I_F = A^{**}AT^2 \exp\left(\frac{-q(\Phi_b)}{kT}\right) \tag{2.1}$$

Where A** is the Richardson constant, A is the electrical active cross section area, Φ_b is the Schottky barrier, T is the temperature, and k is the Boltzmann constant in eV/K units. Current flowing from the semiconductor to the metal across the interface must also be included. If this reverse current is taken as reference and the saturation current above subtracted, image force lowering included, and a correction for the non – ideality of the device also added, we get the following expression for the forward bias current:

$$I_F = A^{**}AT^2 \exp\left(\frac{-q(\Phi_{b0} - \Delta\Phi)}{kT}\right)\left[\exp\left(\frac{qV_F}{nkT}\right) - 1\right] \tag{2.2}$$

Where $\Delta\Phi$ is the image force lowering of the barrier, V_F is the forward bias, and n is the diode ideality factor. Image force lowering is expressed as follows:

$$\Delta\Phi = \left[\frac{q^3 N_A \left(-V_F + V_{bi} - kT/q \right)}{8\pi^2 \varepsilon_0^3} \right]^{1/4} \tag{2.3}$$

Where q is the charge of an electron, N_A is the dopant density, V_{bi} the built in voltage, and ϵ_0 is the CNT dielectric constant. Using the above equations, it is also common to define the activation energy of the MS interface is in terms of Schottky barrier and applied bias:

$$E = \Phi_b - V_F/n = \Phi_0 - \left[\frac{q^3 N_A \left(-V_F + V_{bi} - kT/q \right)}{8\pi^2 \varepsilon_0^3} \right]^{1/4} - V_F \tag{2.4}$$

Note that the above equations are for a MS junction in forward bias, and that simple reversal of the sign on V_F and reversal of the reference direction so that the saturation current is positive yields the reverse bias equations.

In standard MS junctions, there exists an 'interface' space charge region in where bulk electrical and physical properties no longer hold true. Theoretical calculations estimate this interface length to be on the order of 1 – 2 nm [68-70], which interestingly is equivalent to the CNT diameter (Although the effects of such length similarity is not clear).

2.2 POOLE FRENKEL EMISSION AND HOPPING CONDUCTIVITY

Poole Frenkel (PF) emission, named for Y. Frenkel's [71] use of an empirical electrical breakdown relationship early noted by H.H. Poole, describes the emission of trapped carriers from localized states via thermal or electric perturbation. The phenomenon is typically associated with the bulk of an insulating material; however it can occur at the junction of metal –

semiconductor and metal – insulators as well. Figure 2.1 details the differences between Schottky emission and the Poole – Frenkel effect (emission). Under increasingly large electric field application, both semiconductors and metals will eventual display a large increase in conductivity (if material failure does not occur first). This behavior, known as breakdown, was originally described by H.H. Poole, where conductance was modeled as a function of applied electric field:

$$\sigma = \sigma_0 e^{\alpha E} \tag{2.5}$$

The conductivity can be seen to exponential increase as a function of applied E once certain field strength is reached. Frenkels addition to the theorem incorporated a barrier lowering similar to the Schottky Effect [65] that replaced the "E" in Poole's law with a $\sqrt{E}$. The final relationship is described by:

$$J \propto n_0 V \exp\left[-\frac{q}{kT}\left(\Phi_B - \sqrt{\frac{qV}{\pi d \varepsilon_s \varepsilon_0}}\right)\right] \tag{2.6}$$

This relationship was originally introduced by Frenkel to explain increases in current resulting from illumination of a sample (independent of electric field). In modern semiconductors, PF emission involves defects or impurities in materials producing electron (hole) traps in a material that can escape via thermal emission (similar to explanation in section 2.1). Current variations in these materials, which are typically amorphous oxides, are due to the jumping of electrons (holes) between traps with application of an electric field. The depth (depth is referencing the activation energy) of these traps may be extracted via Arrhenius style plots.

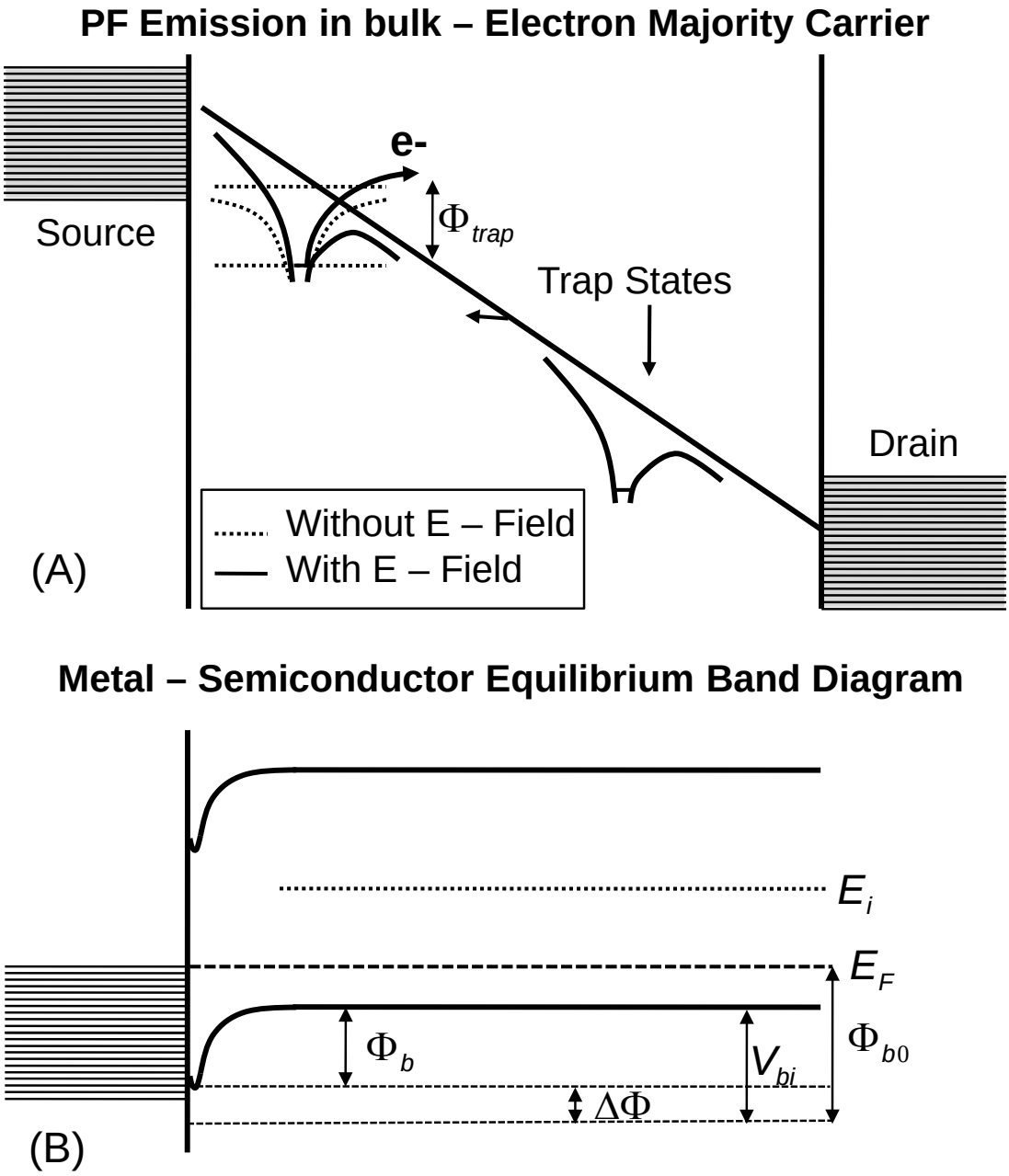

Figure 2.1 (A) Band Diagram of thin film displaying carrier traps (electron traps in this case) with hopping conduction dependent upon applied electric field. (B) Equilibrium band diagram for a metal semiconductor junction, using notation equivalent to that used later in this thesis.

3.0 CNT - METAL SCHOTTKY BARRIER ANALYSIS

3.1 EXPERIMENT SETUP

To characterize metal – CNT junctions accurately and consistently, we utilized a method suitable for comparison of barrier heights between devices. We have fabricated multiple pairs of source-drain contact electrodes, ideally using at least three to five metals, on the same CNT. The process requires longer nanotubes capable of contacts over the range of tens of microns with few defects to prevent frequent diameter and chirality changes for fair comparison of transport mechanisms. Using the same nanotube with multiple metal contacts replicates the multiple fabrication steps utilized in industrial planar processes, as well as subjects all metal contacts to the same conditions. Since measurement of CNT work functions remains difficult in a device configuration, this multi-metal situation allows comparison without worries of variation of this parameter. Two different methods were utilized to fabricate devices for measurement of Schottky barrier height, the first utilized electron beam lithography with an FIB step. The second utilizes only EBL to pattern contact electrodes. Note that deposition, and all other fabrication methods are consistent for the remaining devices analyzed. These processes are compared and contrasted, and the results presented henceforth in the following subsections.

3.2 FIB METHOD SCHOTTKY BARRIER MEASUREMENTS

FIB – method devices were fabricated on an 11 micron long semiconducting SWCNT with a diameter of 2.5 nm, estimated by AFM. An AFM image of such devices and tube is shown in Figure 3.1 with metal electrode composition denoted.

These devices were fabricated with channel length of 400 nm to enable quasi-ballistic transport and allow the assumption of zero voltage drop across this region of the device during the analysis. Current-voltage (I-V) characteristics of Cr, Mo, and Ni devices were gathered for temperatures from 19 K to 300 K in a CCR. At low temperature, the source-drain current was severely limited, indicating that transport was largely due to thermionic emission, and to a lesser extent tunneling through a thin barrier present at the source-CNT interface. This conclusion was also based upon the resulting slope regions of the Richardson plots as can be seen in Figure 3.2 for the Cr contacted device.

In order to discern a dominant conduction model and estimate barrier heights for the contacts, it was necessary to introduce assumptions. For all devices analyzed, it has been assumed that the semiconducting CNT-metal contact behaves equivalently to standard Si/metal contacts described in previous sections. For the devices that were fitted with the Bethe model, this included the assumption that the barrier height is the largest impediment to current, that the channel mobility is high. Unless otherwise noted, each of the FIB devices characterized was done so over the full temperature range of 50 K < T < 200 K, with the model breaking down with tunneling domination below 50 K.

The first device measured is the Cr contacted device denoted by Cr2 in Figure 3.1. Based on differential conductance measurements, the contact resistance was approximately 4 MΩ at room

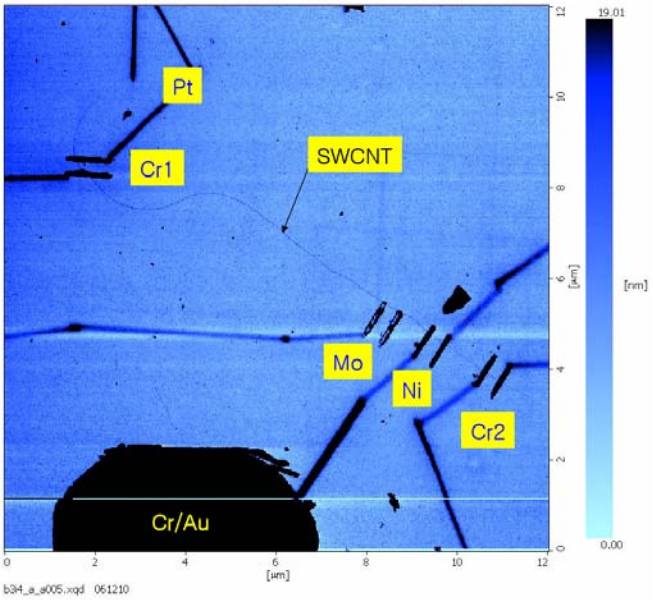

Figure 3.1AFM image of SWCNT contact with metals Cr, Mo, Ni. The small contacting electrodes were connected to probeable pads using FIB deposited Pt lines.

temperature and increased to an insulating 410 GΩ at 30 K for V_{sd} = 0. Richardson plots of this device are shown in Figure 2.2, along with the resulting 38 meV SB height extracted from these plots. This value is considerably lower than what should be expected using a simple work-function difference between the CNT and metal. Cr workfunction is ~ 4.5 eV while the carbon nanotube workfunction, estimated theoretically, should be 4.6-4.8 eV. The bandgap of a CNT with diameter ~ 1.8 can be estimated using the relationship $E_g = \left(.7668 nm/d\right) \approx 0.590\,\text{eV}$ [12]. These assumptions can lead one to assume, if thermionic emission was the only mechanism, of at least a few hundred meV barrier as in standard MS junctions.

A second device, fabricated from Ni metal electrode contacts, displayed similar contact resistances from 3.94 MΩ (295 K) to 94 GΩ (30 K). Utilizing the same activation energy method to extract SB heights for Cr2, we estimate the barrier to be ~ 40.5 meV.

The other unique device analyzed in this FIB sample was a hybrid Mo-Ni FET structure. Although the channel length of this device was over a micron long, the device had similar I-V characteristics to the Ni-only FET structure. Transport characteristics were again consistent with the presence of a Schottky barrier at the source-CNT interface. Contact resistance of this device also increased dramatically for lower temperatures, achieving a low of 3.95 MΩ at 295 K and an insulator-like 280 GΩ, at 30 K. The barrier height is estimated at 41 meV corresponding to the Mo electrode (positive side of the I-V characteristics).

The greatest variation in performance among the FIB – fabricated devices came from device Cr1. This device was fabricated on a curved section of the SWCNT and displayed markedly different characteristics from the other devices, including Cr2. For the Cr1 device, contact resistance varied from 4.04 MΩ at 295 K to 4.01 GΩ at 30 K. Instead of the Schottky type conduction mechanism found as in the other devices, low temperature data fit with the Poole – Frenkel model of electron emission governed by equation 2.6. Poole – Frenkel emission is a phenomenon associated with trap – states and is usually found in amorphous materials including oxides. Data regarding this device is shown in Figure 3. A close-up image of the barrier height best-fit estimation along with Arrhenius plots at various drain source voltages for the Cr1 device can be found in Figures 3.2 and 3.3. I-V data for the device was fit to a measured barrier height of 24.5 meV at $V_{sd} = 0$ over the temperature range $50 < T < 100$ K.

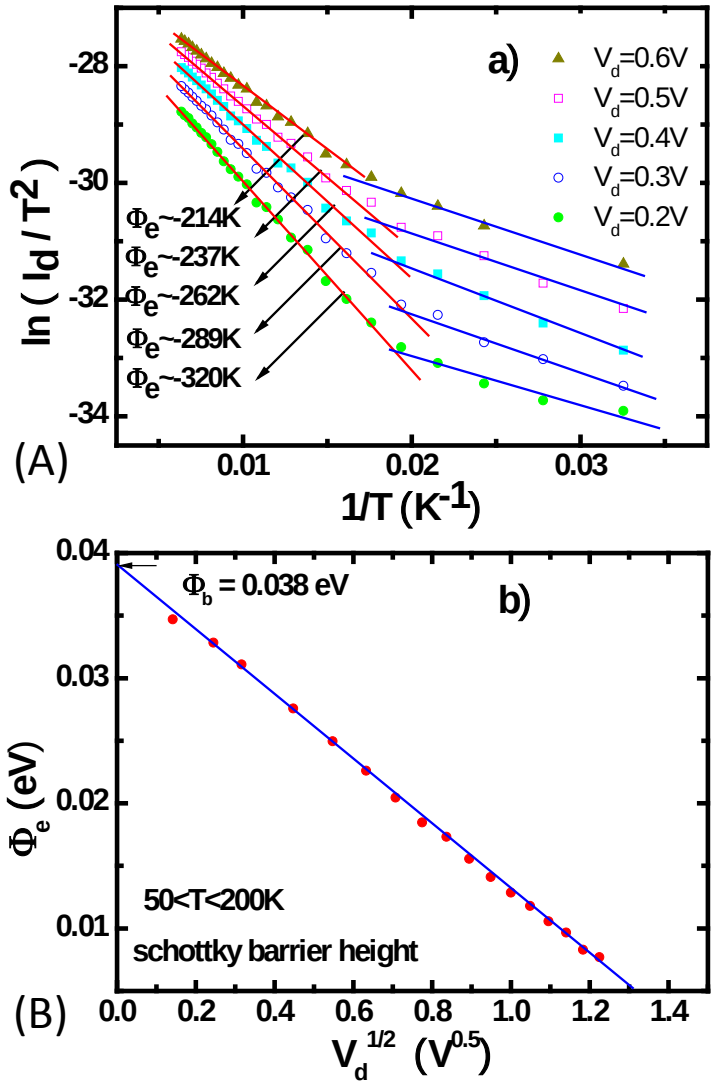

Figure 3.2 (A) ln (Id/T^2) vs 1/T indicates that the gradient of red linear regions describe the Schottky barrier height from 50 K to 200 K at V_d (0.2~0.6 V). (B) Schottky barrier height as a function of drain voltage ($Vd^{1/2}$). Schottky barrier height at zero drain bias voltage (Φ_b) shows 0.038 eV

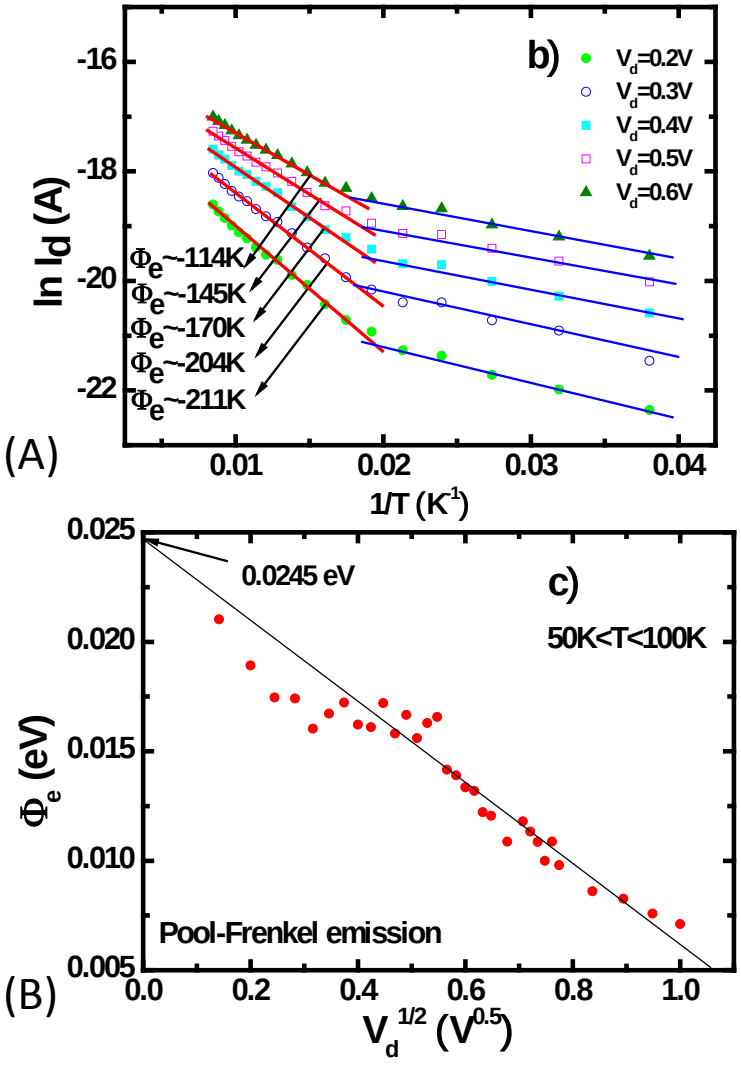

Figure 3.3 (A) ln I_d vs 1/T shows that the gradient of red linear regions indicate the existence of a trap barrier and a very good match to the Poole-Frankel model of conduction for 50 K < T < 100 K at V_d (0.2~0.6 V). (B) Schottky barrier height as a function of drain voltage ($V_d^{1/2}$) In case of Cr2 electrode Schottky barrier height at zero drain bias voltage (Φ_b) shows 0.0245 eV

The resulting plots of each of the above devices are shown together in Figure 6 below. The results indicate that the barrier heights measured depend almost completely on the CNT and not the metal electrode contacts. There also appears to be a prevalence of tunneling attributed to a very thin barrier. To explain the prevalence of tunneling, as well as the observation of Poole-Frenkel emission in the nanotube we make note of the fact that these devices underwent scanning electron microscope (SEM) exposure prior to electrode deposition. SEM imaging was utilized in the very precise location of the tubes after the large Ti/Au pads were deposited. This imaging most likely deposited a small layer of carbon over the nanotube in some areas and decreased the quality of the contact. Devices exhibiting good fit with the Schottky model of conduction likely did not have this carbon deposition at the metal/nanotube interface. It is likely that this SEM exposure introduced charge centers in the back-gate oxide that may generate gap states in the nanotube bandgap to enhance tunneling near the contacts. This would explain the low barrier heights observed. For the Poole – Frenkel emission Cr1 device at the nanotube bend we note the possible existence of two separate phenomenon. Bends in nanotubes are often signs of defects, which have been shown to induce trap states in the forbidden region of the bandgap. This effect can be the source of the Poole-Frenkel emission at low temperature, or it may be the SEM – induced carbon deposition between the metal contact and CNT. This carbon is most definitely amorphous, and the transport mechanism we are observing dominated by hopping in this insulating region. Both situations are likely, however the existence of this mechanism only in the bend of the nanotube lends credibility to the defect induced gap state model of the traps.

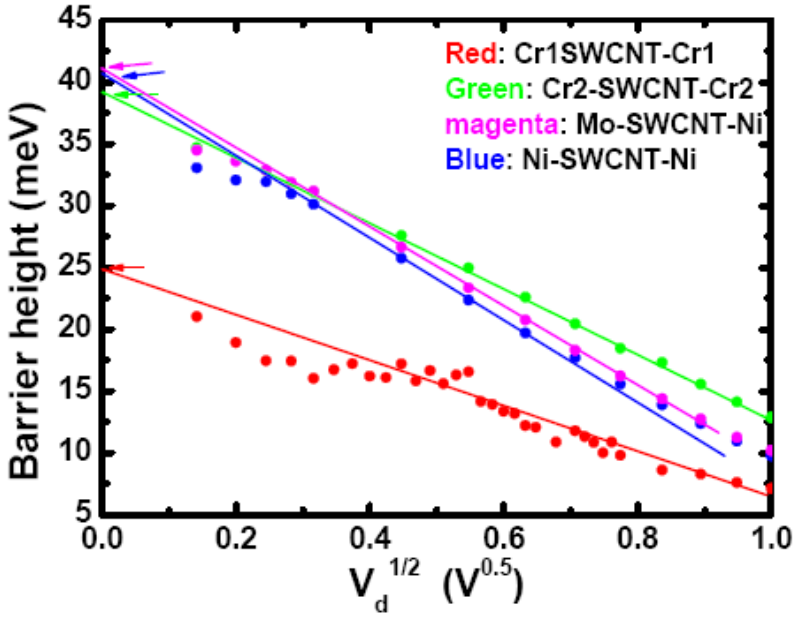

Figure 3.4 Barrier height data for the Cr1, Ni, and Mo – Ni devices the barrier height was found utilizing the Schottky model from 50 K to 200 K. The Cr2 device utilized the same relationship for barrier height, but exhibited Poole – Frenkel type transport for 50 K to 100 K as opposed to the basic Schottky model.

3.3 E-BEAM LITHOGRAPHY FABRICATED CNT TRANSISTORS

To counter the creation of Poole – Frenkel emission and reduce the possibility of trap generation near the CNT contact, an all EBL method was adopted. No e-beam exposure was performed on the nanotubes and AFM was utilized in all situations for precise location of CNT. Again using T-CVD grown nanotubes, probe pads and lead lines on the sample were first patterned and e-beam evaporation used to deposited Ti/Au (5 nm / 35 nm). This was followed by an AFM imaging step to locate the desired CNT more precisely. Repeated ebL patterning and evaporation of metals was performed to deposit Ni, Pd, Cr, Ag, and Ti/Au contact electrodes to the CNT as shown in Figure 3.5. Post AFM images showed that two CNT were in fact present in the primary area of the electrodes, but spacing between electrodes and bad contacts prevented both CNT from creating conducting paths between single pairs of electrodes. After fabrication, we chose to focus attention on analysis of the Schottky diode Pd/Ag contacted CNT. Using low temperature I-V and gate measurements in a CCR, activation energy measurements and nonlinear curve fitting were performed to fit the device to a thermionic emission Schottky diode model.

Using this asymmetric work function setup – the Pd source was ohmically contacted to the nanotube while the Ag electrode served as p-type barrier for holes injected from the CNT to the drain. MS thermionic emission theory is easily applied since the applied potential across the device occurs almost completely over the source contact. This is in contrast to symmetric devices where there is a voltage drop across both contacts that is difficult to estimate or measure without sophisticated AFM modes. A theorized band diagram of the device using the above assumptions is shown in Figure 3.6. The model we utilized takes into account built – in potential, image force

lowering, the ideality factor, and Fermi level position. The program Origin was used for all curve fitting and plotting, particularly the use of the nonlinear fitting functionality.

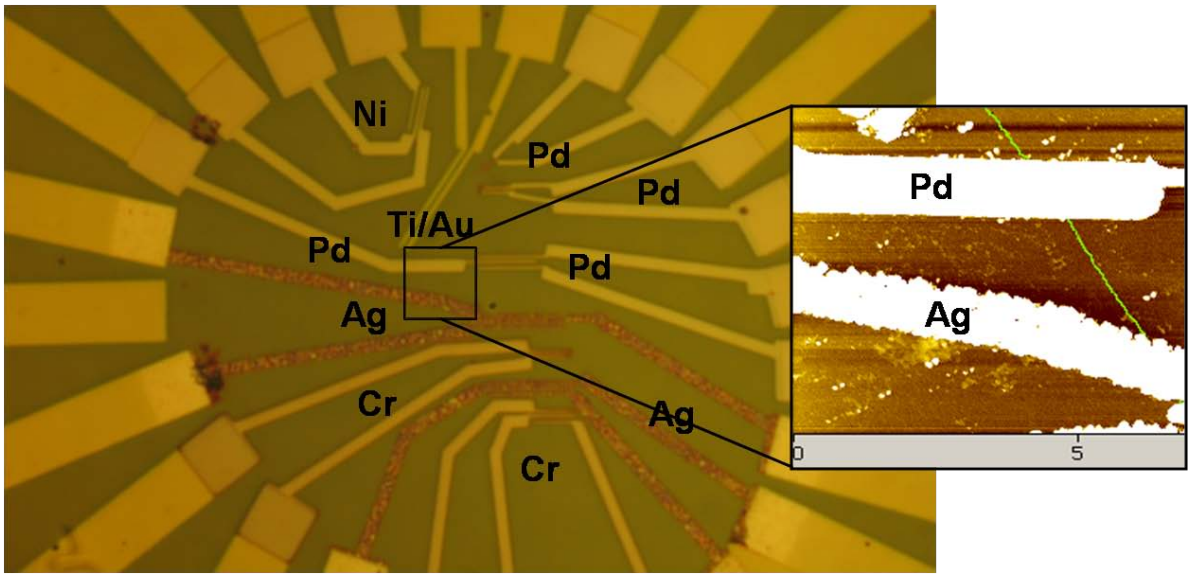

Figure 3.5 – Optical image with metal labels for each electrode deposited on the CNT. The primary device of interest in this setup is the Pd/Ag diode – with the green line in the inset indicating the location of the CNT.

Using log (I_{sd}) vs V_{sd} the constant contact resistance of the Pd source contact was first extracted (assumed Ohmic and therefore constant R_C). The potential drop across the drain Ag contact was then equal to $V_F = V_{sd} - I_{sd} R_C$. This data was used in the equations for forward and reverse bias in equations (2) through (6) to find all relevant values in the equilibrium band diagram.

Using Richardson plots for the forward bias regime shown in figure 3.6, the activation energy was extracted as a function of V_F using the slopes over the temperature range 250 K < T < 300 K. The intercepts from the Figure 3.6 (C) provide the product of the Richardson constant and electrically active area. Both the activation energies and Richardson constant are plotted as a

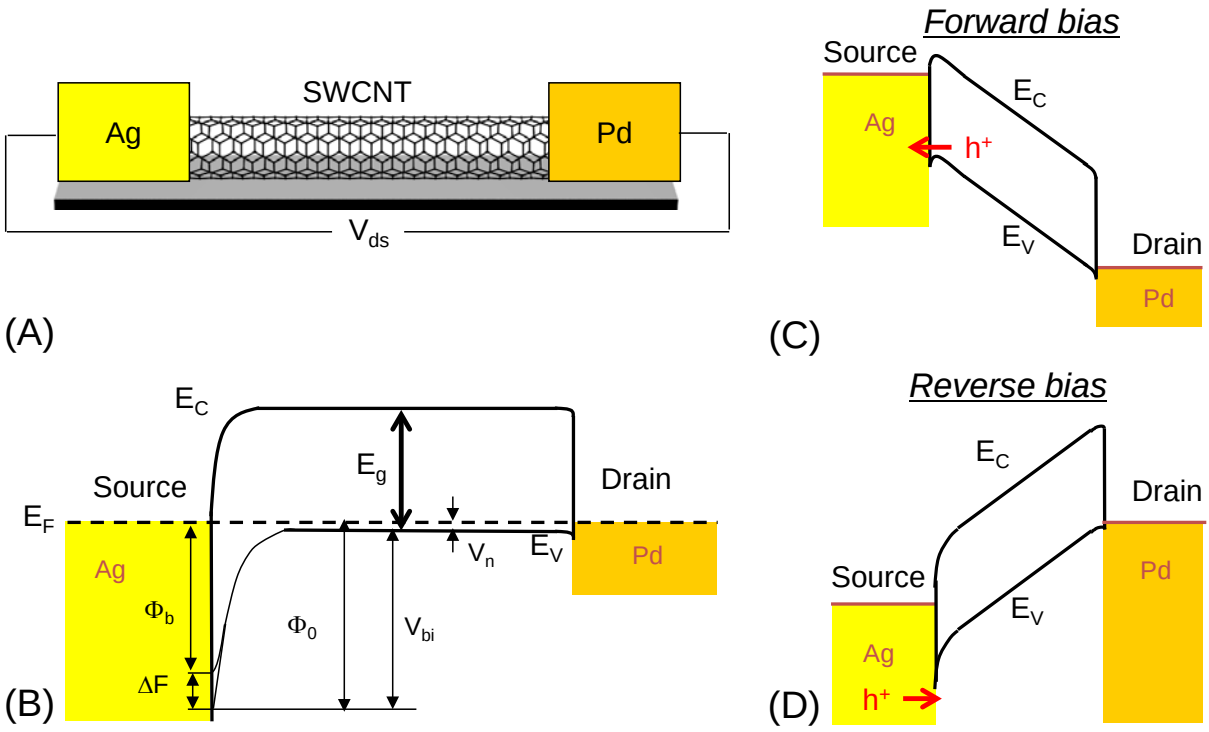

Figure 3.6 – Band Diagram of Ag/Pd Schottky diode fabricated on a single semiconducting CNT. (A) Device schematic. (B) Equilibrium band diagram. The Pd contact is assumed ohmic. (C) Forward bias current is dominated by holes traversing a bias – dependent (and gate – dependent) barrier at the Ag contact. (D) Reverse bias – current severely limited by the constant height barrier at the Ag – CNT contact preventing holes from being injected from the source electrode.

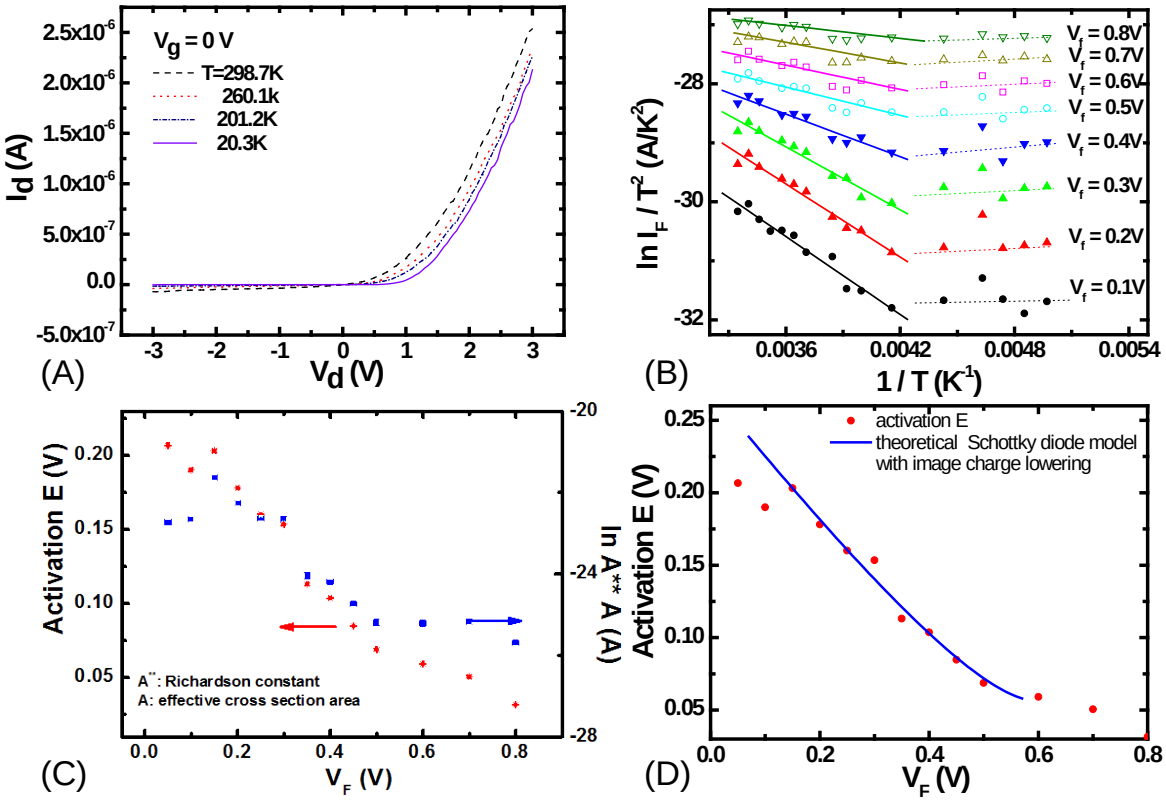

Figure 3.7 (A) I_d-V_d curves at the temperature range from 20K to 300K were measured in the evacuated chamber of the CCR. (B) Activation energy plots ln I_F/T^2 vs. 1/T. (C) Slopes and the intercepts in the linear range of (B), in terms of 1/T with some negative slopes (250K<T<300K), used to extract barrier constants at fixed forward biases. (D) Using the resulting Activation E vs. V_f curve, we can extract further information by fitting with theoretical model.

function of V_F in Figure 3.6 (D). These results were then fit to the theoretical Schottky model from equation 2.2, including the effects of image charge lowering. This analysis was not possible for devices utilizing same metal contacts, but due to the large current anisotropy in this Schottky device, all barrier data was extractable.

From the theoretical model, using Origin for the non linear curve fitting, data including the built in voltage (V_{bi}), intrinsic barrier height Φ_{b0}, SB height Φ_b, Fermi level positioning $E_F - E_V$, ideality factor 'n', and image force lowering $\Delta\phi$. These curve fitting efforts are shown in Figure 3.7. After find V_F, we generated Richardson plots from the low temperature data, and were able to find activation energy as well as the product of the Richardson constant A** and active area A. Using the activation energy, we used nonlinear curve fitting in Origin to fit the resulting data to the theoretical Schottky model. The resulting data is displayed in Table 1. It can be seen from the values that image force lowering plays an extremely significant role in the contact barrier height. Results from the fitting indicate that $\Delta\Phi \sim .1\text{eV}$.

Table 1 Ag – CNT Schottky Barrier Parameters

Intrinsic Schottky Barrier Height Φ_0	$\approx 0.37 \pm 0.01(eV)$
Image Charge Lowering $\Delta\Phi \ (V_F = 0)$	$\approx 0.10 \pm 0.01(eV)$
Schottky Barrier Height $\Phi_b \ (V_F = 0)$	$\approx 0.27 \pm 0.01(eV)$
Built-in Potential V_{bi}	$\approx 0.28 \pm 0.01(eV)$
$E_F - E_V$ for SW-CNT	$\approx 0.09 \pm 0.01(eV)$
Ideality Factor 'n'	$\approx 2.10 \pm 0.01(eV)$

It is also very clear that further exploration into asymmetric work function contacted metal – CNT – metal devices is required to quantify our results. The results presented using the much more complex nonlinear curve fitting are certainly more believable than the almost

constant 40 meV results for each SBH in the FIB devices. This lends us to believe that there is CNT dependence in the FIB case that may be a result of the fabrication process. The use of SEM imaging in the FIB devices appeared to be the root cause of the lower barrier heights and PF emission, therefore in further study of CNT devices this factor was explored via a controlled nanotube electron irradiation examined in the following sections.

4.0 ELECTRON IRRADIATION INDUCED POOLE – FRENKEL EMISSION

Conduction mechanisms in CNT devices are widely assumed to be ballistic in nature if the channel length is less than the mean free path (λ_{mfp}) quoted in the literature. Typical values of λ_{mfp} are a micron or greater [72,73], hence e-beam lithography is often utilized to fabricate site – specific devices with critical dimensions of 500 nm or less. Often, and even previously mentioned here for Schottky barrier height estimations, the channel is assumed ballistic (Or with a constant resistance) simply because the analysis becomes increasingly difficult otherwise.

Here we present an argument relating the fixed charge from electron irradiation, in doses comparable with e-beam lithography exposure, to the formation of a variable hopping mechanism in carbon nanotubes. The Poole – Frenkel emission trap barrier model is utilized to analyze the effects of the charge on semiconducting and metallic CNT, with an adjustment to the theory to account for inconsistencies. The results of irradiating semiconducting and metallic CNT induce very different results effecting performance metrics both positively and negatively in a number of ways that will be discussed below.

CNT field-effect transistor (FET) devices are fabricated on ~ 0.5 cm long aligned along the gas-flow direction by laminar-flow T-CVD method. An e-beam lithography method is employed for the patterning and e-beam evaporation is performed for all metal deposition. After FET fabrication, select devices are covered with a negative resist layer while other unwanted nanotubes are destroyed by O_2 plasma etching. Figure 4.1 illustrates a device diagram including

this resist layer, as well as an AFM image of a sample after the resist was removed with a stripper. During e-beam exposure of the negative resist, the carbon nanotube channel is irradiated with a dose of ~ 350 μC/cm^2 electrons accelerated at 20 keV. The dose and acceleration voltage are far less than the 100 keV for electrons (or much lower for heavier ions) that was suggested in the literature to induce physical defects in the nanotube structure [74-77]. The effects of electron irradiation have been suggested elsewhere including the concept of a reversible insulator transition in metallic CNTs under certain doses [78]. Although no physical atomic damage is caused to the CNTs, thermally grown 800 nm SiO_2 back gate oxide is a well – known acceptor of electrons to produce quasi-fixed negative charges near the carbon nanotube structure [79]. The negative e-beam resist was utilized as a protective layer during the plasma etching of unwanted nanotubes and is another source of negative charge in the vicinity of the nanotube that likely enhances the oxide charge effect.

Hf and Ti metals are utilized for the source and drain contact electrodes due to their good CNT contact properties [33] and the ability to evaporate these metals in an e-beam evaporator. In the pool of ~25 devices measured at room temperature, the majority exhibited contact resistances in the hundred kΩ range. Simple Richardson plots (not shown) were also considered to examine whether thermionic emission over a contact barrier was the dominant factor contributing to the effects. In all cases the model failed with the plots producing positive slope – an indication that the transport was not simple thermionic emission over a contact Schottky barrier. It is hypothesized that the tunneling is the prominent contact phenomenon as suggested by Appenzeller and Chen *et al* [61].

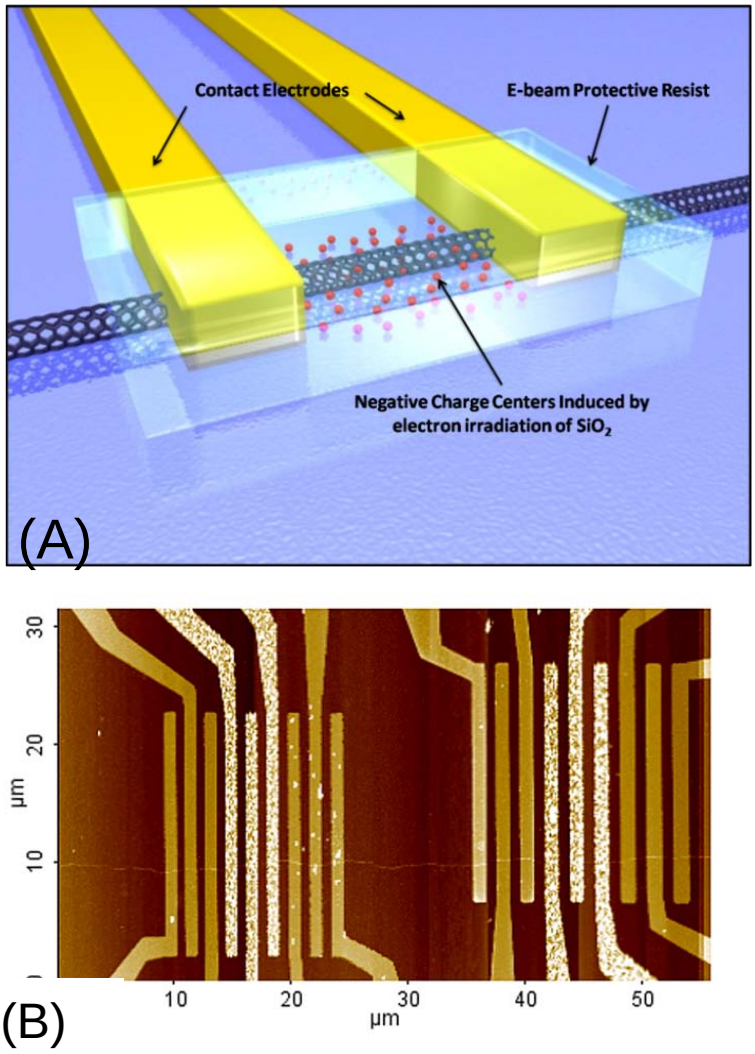

Figure 4.1 (A) 3D diagram of metal – CNT – metal FET devices with protective resist cover. Red spheres indicate the presence of semi-mobile charge centers in the oxide resulting from electron irradiation. (B) Example AFM image of CNT – device layout. The scan was performed after removal of negative e-beam resist, and the one continuous nanotube is visible.

CNT transistor characterization and low-temperature measurements were performed in an evacuated closed-cycle refrigerator (CCR) from 25 to 300 K. The temperature step size of 5 K was utilized over this range, with a hold time of 10 minutes at each temperature to provide sufficient return to thermal equilibrium in the CCR chamber. During this process, the devices remained covered with negative e-beam resist. This layer aides in the retention of irradiated charge as described above and reduces environmental impacts from the evacuated chamber. The CNT FETs measured and analyzed here are from two different samples fabricated at the same time and with the same conditions. Devices on the same nanotube showed similar behavior, the devices were chosen here to compare/contrast the differences in metallic and semiconducting CNT.

4.1 CHARACTERIZATION

The first device considered is a Ti – CNT – Ti FET device with a single semiconducting nanotube serving as the channel. This device displayed $I_{ON} \sim 1.2 \times 10^{-5}$ A at $V_{sd} = 1$ V (300 K), and an on/off ratio = 10^3, as shown in Figure 4.2. Furthermore, significant hysteresis is observed in the gate sweep, an indication that external charge is present near the nanotube. Previously this hysteresis was attributed to water molecules [80], although the previous study was performed for free standing devices with significantly reduced substrate interaction. Devices were also subject to a 200 ^{o}C annealing for 30 minutes while covered with photoresist prior to O_2 plasma that should have reduced hysteresis had water been the primary contributor. Although the presence of water vapor or other molecules still may have increased hysteresis, our samples displayed the behavior well below the freeze-out temperature of oxygen (50K). Therefore, we suggest the

hysteresis is substrate interaction effect enhanced by the e-beam exposure. This effect is twofold – the SiO_2 charge can screen the back gate field, and the creation of insulating regions can induce charge accumulation in the CNT at the bulk – insulator boundaries. The charge accumulation acts similarly to the water effect previously noted. Devices without electron exposure displayed hysteresis, but the difference was noteworthy with the unexposed devices showing significantly less hysteresis.

I-V measurements of the Ti – contacted device exhibited a linear fit to the PF model for $V_{sd} > 0.4$ V when plotting $\ln\left(I_{sd}/V_{sd}\right)$ vs. $\sqrt{V_{sd}}$. Details of the fitting can be found in figure 4.2, where the increasing slope of the lines for increasing V_g suggests a gate bias dependence on the trap-barrier height. The data were subsequently fit using Arrhenius plots over the temperature range 100 K – 300 K to find the trap barrier heights. A strong gate modulation effect on the barrier heights is observed, as shown in figure 2C, with a maximum height occurring at V_g = 15 V (~79 meV) and a minimum at V_g = 0 V (~ 2 meV).

A second metallic CNT-dominated device with Hf contacts was also analyzed. This device displayed weakly ambipolar gate sweep behavior with an on/off ratio < 10 at room temperature. The location of the switch in majority carrier occurred near V_g = 3 V as can be seen in figure 4.3 as the presence of an off-state in the gate sweep. It is not clear if the device contained more than one metallic CNT or if a very small pseudo bandgap opened from the electron irradiation perturbation.

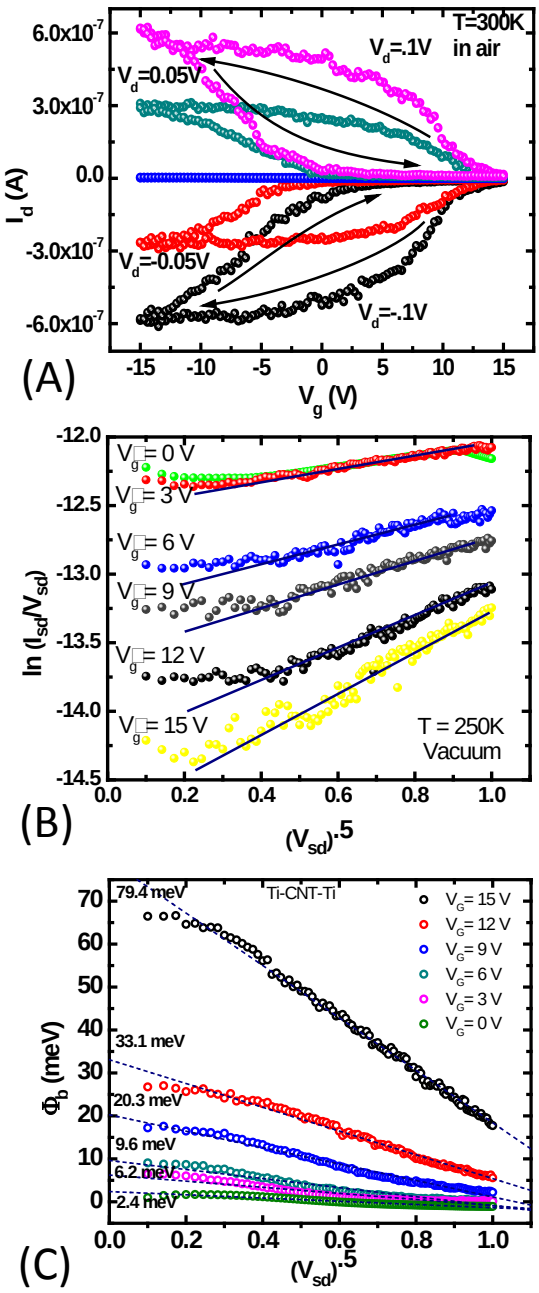

Figure 4.2 (A) Ambient gate sweep of Ti – CNT – Ti FET device. (B) Fit of device in (A) to Poole – Frenkel theory. (C) Trap barrier height estimation fitting found via low temperature measurements and subsequent Arrhenius plots.

The Hf – CNT – Hf device also had significantly lower I_{sd} ~ 60 nA for V_{sd} = 1 V (V_g = -15V), as compared with the Ti – contacted semiconducting device. This suggests that the barrier height for hopping of metallic device is higher than that of semiconducting CNT. The Hf FET device exhibited a good fit when matched with the PF emission model for 3 V < V_{sd} < 9 V for -15 V ≤ V_g ≤ 15 V, over the limited temperature range 240 – 300 K as shown in figure 3B. As could be hypothesized by the switch in majority carrier at V_g ~ 3 V, this voltage was the location of the largest observed trap height at V_{sd} = 0 V with $\Phi_b = 172$ meV – significantly larger than that of the semiconductor CNT. Also contrary to the semiconducting case, the barrier heights did not saturate at 0 meV for V_g << 3 V or V_g >> 3 V. Both positive and negative gate voltages saturated the barrier heights ~ 65 meV.

4.2 DISCUSSION

To show the large differences in barrier heights, as well as the significance of the positive and negative gas bias for the weakly ambipolar Hf device, both sets of data are plotted together in Figure 4.6. Prior to saturation, it can be clearly seen that by plotting on a logarithmic scale, the barrier height displays a linear relationship. The separated fit lines for both the hole and electron majority carrier trap heights are shown for the Hf device, with a special point occurring near V_g = 3 V. For negative gate voltages, for the metallic or semiconductor case, the hopping is dominated by holes hopping into electron-filled traps in the CNT insulator region. As the gate voltage is increased, the majority carrier is switched to electrons hopping into empty traps.

The difference in metallic and semiconducting e-beam exposed CNT devices is explained via a model based upon metal – insulator – metal (MIM) hopping and semiconductor – insulator

- semiconductor (SIS) junctions while considering the CNT electronic DOS. Metallic tubes have a linear energy dispersion relation near the intrinsic Fermi level estimated by: $E(k) \propto |k - k_F|$.

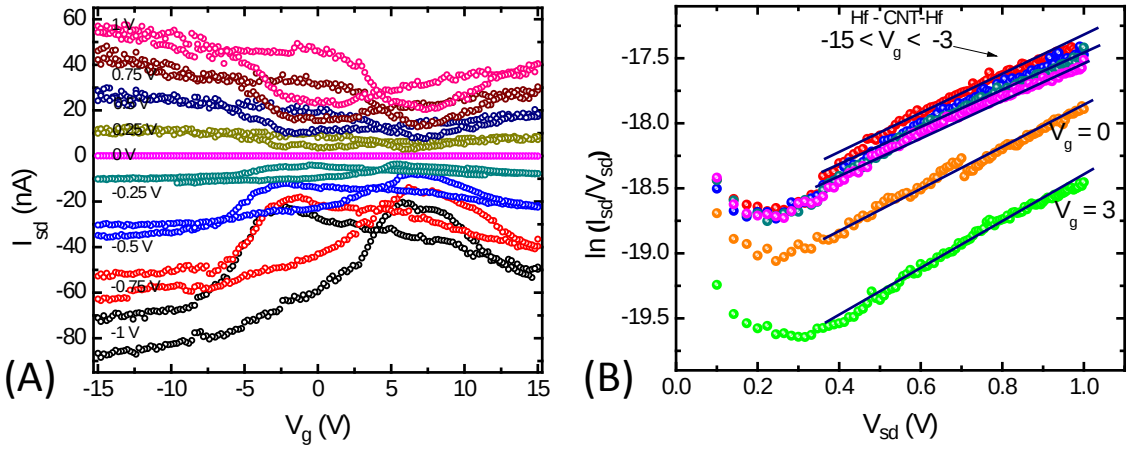

Figure 4.3 (A) Gate sweep in ambient conditions of Hf – CNT – Hf device. (B) Fit of I_{sd} vs V_{sd} to the Poole – Frenkel trap emission equation.

The first van Hove singularity (VHS) is typically located a significant distance away from the Fermi level, and the lowest unoccupied state is not located near the vHs. Instead, the lowest unoccupied state is located in the linear region where the limited (but nonzero) number of energy states exists. The DOS at this point may also be further depleted by the opening of a pseudo band gap resulting from perturbation from the substrate electric field. This can be easily explained via a wavefunction localization model. The perturbation on the electronic band structure in a localized region appears as a pseudo-quantum dot via charge quantization not only radially – but now along the length of the CNT. The result on the band structure is similar to taking a cookie – cutter to the electronic band structure resulting in a finite set of allowable states in the insulating region of the CNT. These states are the resulting trap states observed in the

analysis presented here. Figure 4.4 details intrinsic and perturbed allowed electronic states in the graphene Brillouin zone.

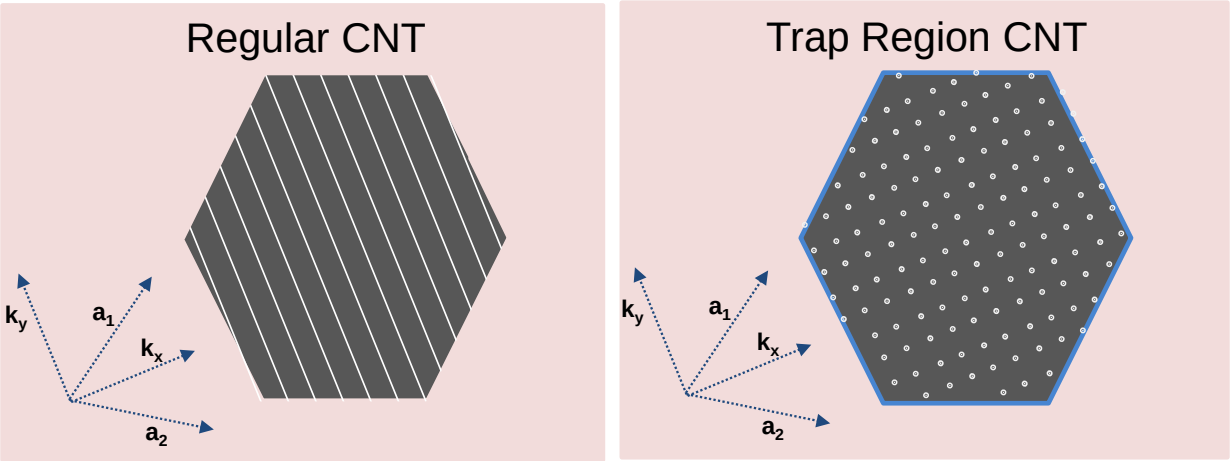

Figure 4.4 Graphene/CNT Brillouin zone under usual radial energy quantization conditions (lines indicate allowed k-space values). When this condition is further applied in the length of the CNT, the allowed energy bands are reduced to a discrete set of states viewable as dots in the Brillouin zone above.

Due to the unvarying DOS at the Fermi level position, gate voltage variations induce no extreme carrier density changes in the gate sweeps (Although a small On/Off ratio is visible). At the location of a majority carrier change, at a special point near V_g = 3 V, a noticeable spike in the trap activation energy occurs.

The exponential relationship near the special point may provide further insight into the nature of the hopping. We suggest that the hopping states in the insulating region are away from the intrinsic Fermi level of the CNT. This assumption is introduced as a side-effect of energy quantization in the insulator region along the length direction of the CNT. In such a case, the DOS would be limited to a discrete number of energy levels observed as hopping levels in the current model. As the Fermi level crosses through the insulator bandgap the barrier height modulation is determined by the energy difference between the gap states and the CNTs Fermi

level. This is exemplified in figure 4.5 where the insulator traps are shown as gap states in the insulating regions and the hopping level to Fermi level gap is denoted by Φ_B. The exponential relationship with respect to V_g is a reflection of a barrier dependent on the energy difference between the trap state and the initial energy level.

However, the barrier height saturates at a minimum for metallic CNT and different phenomenon dominates. Theoretical calculations [81] indicate hopping lengths and conductivity are affected by the variability and magnitude of the DOS. As barrier saturation occurs, the hopping shifts from a difference in energy levels Φ_B to a dependency on tunneling probability similar to the description by Grünewald *et al* [82]. It is hypothesized that a constant, numerically limited DOS induces a shorter localization length. To compensate, a larger total energy barrier denoted $\Phi_b = \Phi_B + \Phi_{sat}$ is induced for wavefunction overlap between the initial energy level in the bulk and the hopping state present in the insulating region. As in a variable-range hopping model, an additional competing factor determined by the hopping distance and localization length can be added to the basic Poole Frenkel model. Equation 2.6 takes the form:

$$J \propto n_0 V \exp\left[-\frac{q}{kT}\left(\Phi_B - \sqrt{\frac{qV}{\pi d \varepsilon_s \varepsilon_0}}\right)\right] \cdot \exp[-\alpha] \qquad (3.1)$$

with $\alpha = \frac{2R}{\xi(V_{sd}, T)}$, R = distance between hopping states, and $\xi(V_{sd}, T)$ the localization length [83]. In metallic CNT, the electron irradiation generates a very small localization length and a decreased carrier wavefunction overlap that aids in the carriers to 'forget' their phase. In pristine CNT, coherent phase transport and wavefunction delocalization across the length of the channel is common and experimentally verified [84-88]. This increased localization and phase memory loss dramatically decreases current carrying capability in metallic CNT. Figure 4.6

shows the dependence on localization energy and hopping and the significant effect of Φ_{sat} on required hopping energy. This concept explains the electron-induced conduction degradation

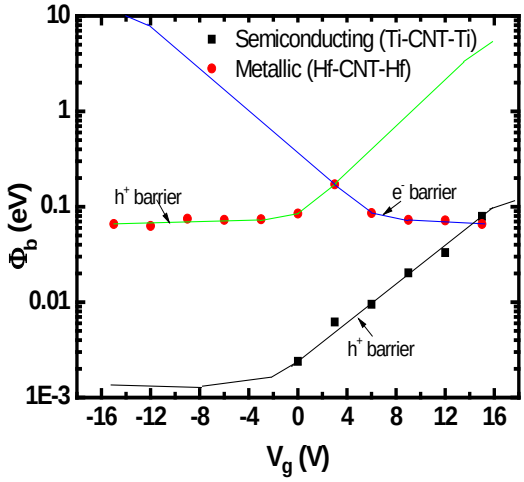

Figure 4.5 Trap barrier heights for the Hf and Ti devices as a function of gate voltage. The Hf device barrier measurements can be split into contributions dependent on carrier type. The exponential barrier relationship is consistent with re-plotted results from Nosho *et al* [89].

observed previously [78]. The V_{sd} and T dependence of α is not clear, but a large T dependence on localization length and carrier 'phase memory' across the insulating regions is hypothesized as the reason why PF emission was observed only for $240 \leq T \leq 300$ K.

In contrast to the metallic case, semiconducting nanotubes have a nonlinear quadratic energy dispersion relation near the valence and conduction band edges described by: $E(k) \propto |k - k_F|^2$. The valence band and conduction band edges dominate conduction mechanism properties – dependent upon contact metal work function alignment and magnitude of V_g applied. The trap barrier height is determined via the difference between the valence band edge vHs and the final hopping state. The valence band of the nanotube is pinned to the insulating region, as shown in figure 5B. After alignment of the Fermi levels, the difference in

the valence band and final trap states determines what energy a carrier must have for successful hopping. Gate modulation shifts the valence band down/up to decrease/increase effective trap barrier height. For large negative gate bias, tunneling through the small barrier to the trap state in the insulator dominates as the vHs of the valence band and trap state are aligned. Semiconducting CNT have a larger localization length/shorter hopping distance due to the exponentially varying DOS with small α. The near – zero barrier height calculated for $V_g = 0$ V is in good agreement with the large I_{sd} of the device in the on – state. The current in semiconducting CNT was consistently larger than metallic devices measured due to the hypothesized large α value in the metallic devices.

The exponential dependence of the barrier height on gate voltage for the semiconducting CNT is again synonymous with a trap barrier height dominated by the energy difference between the final hopping state and the initial state. If the previous results by Nosho *et al* [89]. are plotted on a logarithmic access, the same association for Schottky barrier height is observed. Although the nature of the barriers is quite different, the dominant factor is an energy difference between initial and final states, where Fermi level modulation varies the barrier height.

In addition to the channel, the CNT contact region must contain traps/gap states. In the off-state, carriers tunneling through the contact – CNT interface due to the presence of gap states in this region can contribute to I_{sd}. Figure 4.2(A) is consistent with our observation that electron irradiated devices exhibit substantially higher off-state current (nA) than non-irradiated devices. Other devices fabricated via identical methods, on other samples in which optical lithography was utilized instead of EBL for the protective layer showed off current ~ 100 fA, the limit of the measurement system. Furthermore, the inclusion of these gap states may decrease contact

resistance by improving tunneling, but subsequently reduce the on/off ratios possible due to the leakage current and PF emission.

On a control sample, with no SEM exposure of the CNT channel, the hopping behavior was not observed. The hopping behavior was consistent only in devices with electron irradiation of the nanotube channel. Some oxide irradiation occurs at the contacts during e-beam lithography for source/drain patterning, but the dosage is one third the situation investigated here and does not restrict the use of e-beam lithography in device fabrication – so long as no channel irradiation is performed. Even so, strong doses during device fabrication may result in inconsistent barrier heights due to an increase the effect of tunneling/hopping at the contacts. To ensure that the effects viewed were also not leakage current in the SiO_2, devices were fabricated with no CNT crossing the source/drain contacts and electron exposure was performed. Measurements indicated that $I_{sd} \sim 10^{-12}$ A – significantly less than the typical μA device current and consistent with V_{gs} leakage current.

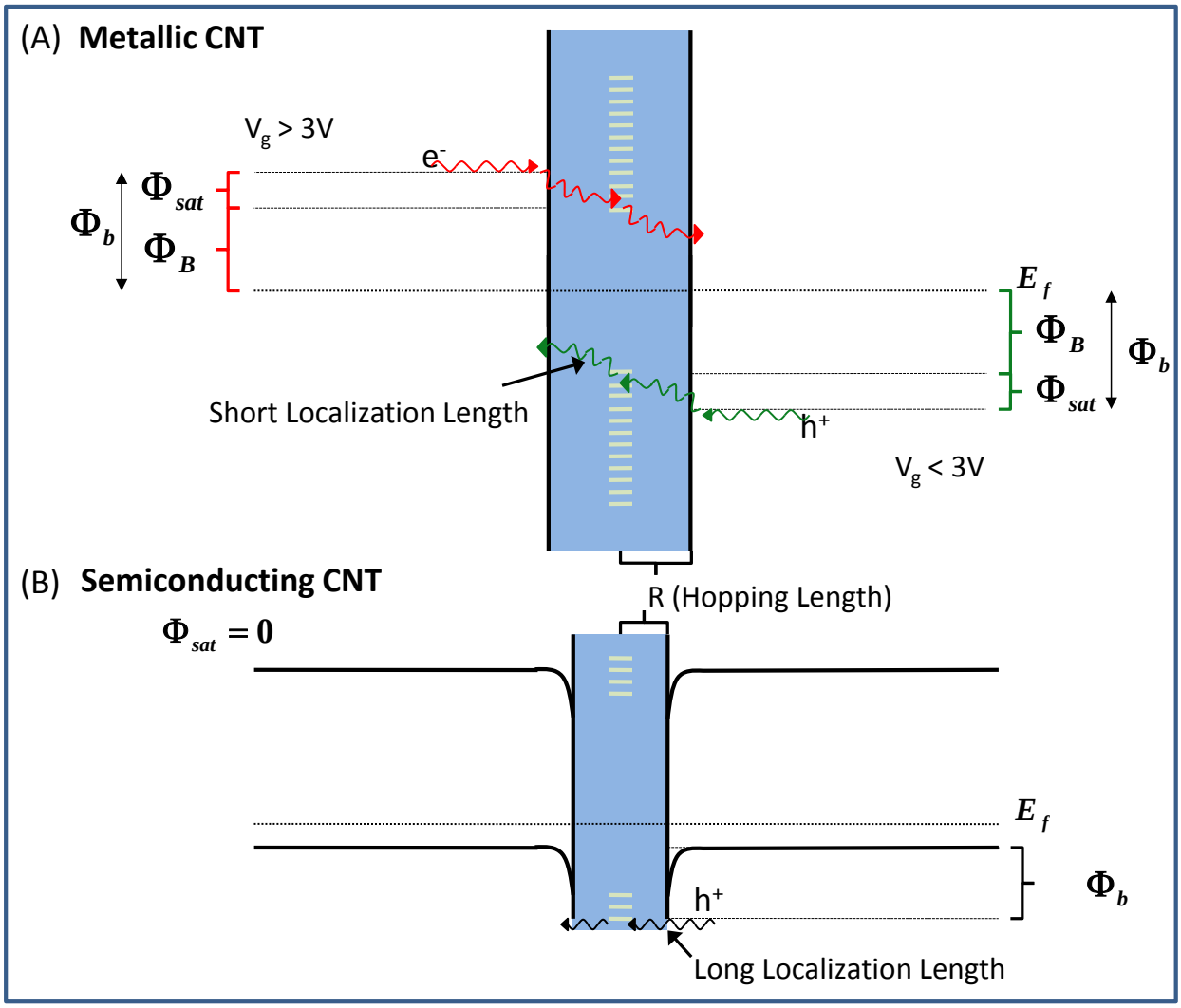

Figure 4.6 (A) MIM CNT junction displaying the difference for applied gate bias of $V_g > 3V$ and $V_g < 3V$. The measured barrier height is broken into saturation and energy gap components with the blue area denoting an electron irradiation induced insulating region of the CNT. (B) Energy diagram of a SIS junction in a CNT. Hopping states included in the insulating regions are denoted by white lines. Large $\frac{\text{hopping length}}{\text{localization length}}$ for the MIM junction requires a large saturation barrier height Φ_{sat} for hopping to occur, while the value is nearly zero for SIS junctions.

5.0 CONCLUSION AND FUTURE WORK

5.1 CONCLUSION

In this thesis, we have presented analysis of CNT contacts and channel conductance under different fabrication and exposure conditions. CNT transistors were fabricated by both an EBL and FIB hybrid technique, as well as an all EBL technique. While initial device were grown on CNT with lengths less than 100 μm, laminar flow growth has now enabled us to grown aligned nanotubes limited only by the sample length (~1 cm). This new method was utilized in the study of electron irradiation effects in the CNT channel. By using such a method, we were able to test nearly 50 devices on a single nanotube.

The results of the analysis indicate that carbon nanotube contacts are strongly dependent upon the CNT, dependent upon fabrication method. Silver contacts have an estimated barrier height of .27 eV on clean nanotubes (not electron exposure). Meanwhile, if strong electron exposure is performed, metal contacts are less important, and the dominate factor becomes trap generation in the CNT channel. This factor should be of keen interest to utilizing CNT in electrical devices, particularly transistor or diode devices where on/off ratios and current anisotropy are important benchmarks.

The effect of electron irradiation in doses comparable to that utilized in EBL showed the creation of carrier traps along the CNT channel. This result was explained utilizing the PF

excitation model with a correction factor to account for varying localization lengths possible in materials with wildly non linear DOS. This electron exposure effect is of importance to nano fabrication, since it presents a critical argument for the use of EBL in certain situations. One example is Graphene Nanoribbons – which are often fabricated with a covering mask patterned via EBL. This exposure may alter the conduction of graphene as it did here with CNT devices, and phenomenon misdiagnoses can easily occur.

5.2 LIST OF RESULTING PUBLICATIONS

[1] Perello, D.; Yu, W. J.; Bae, D. J.; Chae, S. J.; Kim, M. J.; Lee, Y. H.; Yun, M. Analysis of hopping conduction in semiconducting and metallic carbon nanotube devices. *Journal of Applied Physics* **2009,** *105* (12), 124309-5.

[2] Perello, D.; Dong, J. B.; Kim, M. J.; DongKyu, C.; Seung, Y. J.; Bo, R. K.; Woo, J. Y.; He, Y. L.; Minhee, Y. Quantitative Experimental Analysis of Schottky Barriers and Poole Frenkel Emission in Carbon Nanotube Devices. *Nanotechnology, IEEE Transactions on Nanotechnology* **2009,** *8* (3), 355-360.

[3] Perello, D.; Kim, M. J.; DongKyu, C.; Gang, H. H.; Dong, J. B.; Seung, Y. J.; Young, H. L.; Minhee, Y. Schottky barrier engineering in carbon nanotube with various metal electrodes. *Proceedings of 7th IEEE Nano, Hong Kong* **2007**; pp 189-193.

5.3 FUTURE WORK

In this thesis it is shown that extraction of Schottky barrier information is indeed possible for CNT – metal contacts. The method of using only diode based devices where one contact is ohmically contacted appears to be the only realistic method of extracting barrier information. For double – barrier FET samples, barriers may be extracted, but the resulting voltage drops across each of the contacts may not be trivial– and therefore resistance at low applied bias is also non-trivial for both contacts.

The next logical step for this research is to use the knowledge acquired in the fabrication and characterization of these previous devices to better analyze transport models in CNT as well as other nanowires and nanotubes. One serious difficulty in using the methods of this thesis is the initial conditions for the curve fitting. In nonlinear curve fitting – where under defined or over defined equations are often present, results are not always consistent when different initial conditions are utilized. Efforts were made to remove this dependency in our analysis, but the large number of unknowns in the curve fitting innately creates an element of uncertainty (even if this uncertainty doesn't show up statistically in the analysis in the form of standard deviations or error bounds).

This factor alone is one reason for exploring SB phenomenon in CNT with a variety of metals and nanotubes. An element of consistency in the factor A*A may allow improved accuracy when estimating barrier heights. Very preliminary work of ours suggests more consistent values of A*A, with Hf contacts producing values between ln(-26) and ln(-27).

Current and future work is based upon using similar methods to that in the all EBL SBH analysis section, and implementing curve fitting with the similar parameter values to that of the Pd/Ag Schottky diode. Success on this research front will be extremely valuable to any

researchers and scientists interested in logic devices or controllable contacts to Nanoscale devices. The results of this work will aid in determining dominant contact factors, such as metal wettability, valence band structure, lattice structure, or environmental concerns – each of which will aid in the development of devices based on CNT and other nanowires.

APPENDIX A

THERMIONIC EMISSION AT MS INTERFACE – DERIVATION OF BETHE THEORY

Following the analysis present by Sze [6], which is a report of the original work performed by Bethe in 1942 [90]. Three assumptions utilized in this approximation are (1) the thermal energy kT is smaller than the barrier height $q\Phi_B$ and (2) net current does not affect the junction equilibrium. First considering the current from the semiconductor to the metal, we assume only those electrons with sufficient thermal energy can be driven via an electric field across the potential barrier. The current is thus a product of the carrier velocity and the charge per carrier integrated over all energies greater than the barrier height:

$$J_{S\to M} = \int_{E_F+q\Phi_B}^{\infty} qv_x dn \tag{A.1}$$

With $E_F + q\Phi_B$ the minimum electron energy to surmount the barrier into the metal and v_x the carrier velocity. We can express the electron density dn as a function of the density of states and distribution:

$$dn = N(E)F(E)dE \tag{A.2}$$

$$dn = \frac{4\pi(2m^*)^{\frac{3}{2}}}{h^3}\sqrt{E-E_C}\,e^{\left[-\frac{(E-E_C+qV_n)}{kT}\right]}dE \tag{A.3}$$

Such that N(E) is density of states and F(E the distribution function, m* is the effective mass of electrons (holes) and qV_n is the gap between the Fermi level and the conduction band (or valence band for CNT). If we further assume that the energy of electrons in the conduction band is all kinetic energy, then we can change all variables to be expressed in carrier velocity:

$$\sqrt{E - E_C} = v\sqrt{\frac{m^*}{2}} \tag{A.4}$$

$$dE = m^* v dv \tag{A.5}$$

Substituting back into equation (B.3):

$$dn = \frac{4\pi(2m^*)^3}{h^3} e^{\left[-\frac{(m^* v^2 + qV_n)}{kT}\right]} v^2 dv \tag{A.6}$$

Using $v^2 = v_x^2 + v_y^2 + v_z^2$ and $4\pi v^2 dv = dv_x dv_y dv_z$ and using equations A.1 and A.6

We get:

$$J_{S\to M} = \frac{2q(2m^*)^3}{h^3} e^{\left[-\frac{(qV_n)}{kT}\right]} \int_{-\infty}^{\infty} v_x e^{\frac{-m^* v_x^2}{2kT}} dv_x \int_{-\infty}^{\infty} e^{\frac{-m^* v_y^2}{2kT}} dv_y \int_{-\infty}^{\infty} e^{\frac{-m^* v_z^2}{2kT}} dv_z \tag{A.7}$$

Solving the Gaussian integrals and assuming v_{ox} is the minimum velocity in the x (parallel to CNT axis here) required to cross the barrier we can use the relationship $\frac{1}{2} m^* v_{0x}^2 = q(V_{bi} - V)$ with V_{bi} the built-in voltage, to simplify equation (A.7) to:

$$J_{S\to M} = \frac{4\pi(2m^* k^2)}{h^3} T^2 e^{\left[-\frac{q(V_{bi}+V_n)}{kT}\right]} e^{\frac{qV}{kT}} = A^* T^2 e^{\left[-\frac{q\Phi_B}{kT}\right]} e^{\frac{qV}{kT}} \tag{A.8}$$

Where A* is the Richardson constant is a material independent parameter defined by $A^* = \frac{4\pi(2m^* k^2)}{h^3}$.

Total current is $J = J_{S\to M} + J_{M\to S}$ where the current from the metal to the semiconductor is constant due to a constant barrier height (no potential dependence here – although for inclusion of image force lowering there will be a dependence). The simplest method to find this current is to simply plug in V = 0 for the $J_{S\to M}$ equation. This results in the so called saturation current:

$$J_{M\to S} = A^{*}T^{2}e^{\left[-\frac{q\Phi_B}{kT}\right]} \tag{A.9}$$

Hence the final expression for current is:

$$J_{S\to M} = A^{*}T^{2}e^{\left[-\frac{q\Phi_B}{kT}\right]}\left(e^{\frac{qV}{kT}} - 1\right) \tag{A.10}$$

APPENDIX B

CNT ELECTRONIC BAND STRUCTURE USING TIGHT BINDING WITH ZONE FOLDING APPROXIMATION

The graphene band structure is a hexagonal lattice, with each atom having exactly 3 nearest neighbors. In each carbon atom, we must only worry about the p_z electrons, due to lack of overlap or zero total overlap for all other s, p_x, and p_y electron wavefunctions. Beginning with Shrodinger's Equation:

$$H\Psi(k) = E(k)\Psi(k) \tag{B.1}$$

With H the Hamiltonian, E the energy eigenvalues, and $\Psi(k)$ the corresponding eigenfunctions. Each eigenfunction can further be written as a linear sum of Bloch functions:

$$\Psi(k) = \sum_m c_m \Phi_m(k) \tag{B.2}$$

These Bloch functions are themselves written as linear sums of atomic wave functions. The graphene lattice contains a dual basis, and we shall denote the atoms in the first and second sublattice by the the subscripts "D" and "F". Normallized Bloch functions for the sublattices therefore are:

$$\Phi_D = \frac{1}{\sqrt{N}} \sum_{R_D} e^{ik\cdot R_D} \phi(r - R_D) \tag{B.3}$$

$$\Phi_F = \frac{1}{\sqrt{N}} \sum_{R_F} e^{ik \cdot R_F} \phi(r - R_F) \tag{B.4}$$

With N = number of unit cells, and R_D and R_F the translational lattice vector. Solving the Schrodinger's equation, we substitute in the Bloch functions from equation ( ) and multiply by Φ_D and Φ_F. The resulting linear equations are:

$$\begin{aligned} C_D\left[H_{DD}(k) - E(k)S_{DD}(k)\right] + C_F\left[H_{DF}(k) - E(k)S_{DF}(k)\right] = 0 \\ C_D\left[H_{FD}(k) - E(k)S_{FD}(k)\right] + C_F\left[H_{FF}(k) - E(k)S_{FF}(k)\right] = 0 \end{aligned} \tag{B.5}$$

With $H_{jn}(k) = \langle \Phi_j | H | \Phi_n \rangle$ and $S_{jn} = \langle \Phi_j | H | \Phi_n \rangle$ the Hamiltonian matrix elements and the overlaps of the Bloch functions, respectively. We simply the system of equations by noting that $H_{DD}(k) = H_{FF}(k)$, $H_{DF}(k) = H^*_{FD}(k)$, $S_{DD}(k) = S_{FF}(k)$, and $S_{DF}(k) = S^*_{FD}(k)$ and finding the nontrivial solutions for $E(k)$ that satisfy the 2 x 2 matrix determinant $\det[H - ES]$. This yields:

$$E(k)_{\pm} = \frac{-(-2E_0 + E_1) \mp \sqrt{(-2E_0 + E_1)^2 - 4E_2E_3}}{2E_3} \tag{B.6}$$

With E values as follows, with k variable dropped to ease notation:

$$\begin{aligned} E_0 &= H_{DD}S_{DD} \\ E_1 &= S_{DF}H^*_{DF} + H_{DF}S^*_{DF} \\ E_2 &= H^2_{DD} - H_{DF}S^*_{DF} \\ E_3 &= S^2_{DD} - S_{DF}S^*_{DF} \end{aligned} \tag{B.7}$$

With $E(k)^+$ representing the valence band and $E(k)^-$ the conduction band of graphene. Next we will assume that interactions occur only between nearest neighbors. The quantity H_{DD} is solved first:

$$H_{DD} = \langle \Phi_D | H | \Phi_D \rangle = \frac{1}{N} \sum_{R_D} \sum_{R_{D'}} \left\langle e^{ik \cdot R_D} \phi_D(r - R_D) \middle| H \middle| e^{ik \cdot R_{D'}} \phi_D(r - R_{D'}) \right\rangle \tag{B.8}$$

The nearest neighbor assumptionimplies that for each R_D summed over the second has only $R_D = R_{D'}$, simplifying the equation greatly and allowing us to define a new constant ε_{2p}:

$$\varepsilon_{2p} = H_{DD} = \frac{1}{N} N \left\langle \phi_D (r - R_D) \middle| H \middle| \phi_D (r - R_{D'}) \right\rangle \qquad \text{(B.9)}$$

The matrix element for the Hamiltonian between the D and F atoms is slightly more complicated, but begins with the expression:

$$H_{DF} = \left\langle \Phi_D \middle| H \middle| \Phi_F \right\rangle = \frac{1}{N} \sum_{R_D} \sum_{R_F} e^{ik \cdot (R_D - R_F)} \left\langle \phi_D (r - R_D) \middle| H \middle| \phi_F (r - R_F) \right\rangle \qquad \text{(B.10)}$$

The first sum is simply over N atoms in the lattice, once again cancelling out the 1/N constant. The second sum, however, is done over the three nearest neighbors of each atom R_D. To perform this sum, the vector quantities for the three nearest neighbors (which are defined as $R_{1i,}$ R_{2i}, and R_{3i} here, with $R_{ki} = R_{B(ki)} - R_A$ and k indicating the number of neighbors (1) and i = 1, 2, 3) must be known. These are:

$$R_{11} = \frac{1}{3}(2a_1 - a_2) \qquad R_{12} = \frac{1}{3}(-a_1 + 2a_2) \qquad R_{13} = \frac{1}{3}(-a_1 - a_2)$$

Inserting into equation (B.10) above, and recognizing that the atomic wavefunctions are radial symmetric, the Hamiltonian matrix element becomes:

$$H_{DF} = \left(e^{ik \cdot R_{11}} + e^{ik \cdot R_{12}} + e^{ik \cdot R_{13}}\right) \left\langle \phi_D (r - R_D) \middle| H \middle| \phi_F (r - R_D - R_{11}) \right\rangle \qquad \text{(B.11)}$$

Which can be further reduced by introducing the constant γ_0 and substituting in the vector constants for R_{11}, R_{12}, R_{13} :

$$H_{DF} = \gamma_0 \left(e^{-\frac{1}{3} ik \cdot (a_1 + a_2)} \right) \left(e^{ik \cdot a_1} + e^{ik \cdot a_2} + 1\right) \qquad \text{(B.12)}$$

γ_0 is typically referred to as the tight binding integral. Performing the same analysis for S_{DF}, we get:

$$S_{DF} = S_0\left(e^{-\frac{1}{3}ik\cdot(a_1+a_2)}\right)\left(e^{ik\cdot a_1} + e^{ik\cdot a_2} + 1\right) \qquad \text{(B.13)}$$

With the constant overlap integral $S_0 = \left\langle \phi_A \middle| \phi_{B_{1i}} \right\rangle$. Finally, the resulting energy bands can solutions can be achieved by substituting the values of H_{DF} and S_{DF} (or conjugates) into the E(k) expression of equation (B.7) to get the result (in reciprocal lattice vectors $\mathbf{k} = k_1 \mathbf{k_1} + k_2 \mathbf{k_2}$)

$$E^{\pm}(k_1,k_2) = \frac{\varepsilon_{2p} \pm \gamma_0\sqrt{3 + 2\cos 2\pi k_1 + 2\cos 2\pi k_2 + 2\cos 2\pi(k_1 - k_2)}}{1 \pm s_0\sqrt{3 + 2\cos 2\pi k_1 + 2\cos 2\pi k_2 + 2\cos 2\pi(k_1 - k_2)}} \qquad \text{(B.14)}$$

Note that an even simpler "tight binding approximation" can be performed by assuming that the overlap between atomic wavefunctions at different atoms is zero ($S_{DF} = 0$), and assuming $S_{DD} = 1$. This is a reasonable assumption and significantly reduces the complexity of the energy band equations by forcing $E_1 = 0$ and $E_3 = 1$ [91]. This method is only accurate near the graphene k – points due to trigonal warping effects.

BIBLIOGRAPHY

1. Yu, M. F.; Files, B. S.; Arepalli, S.; Ruoff, R. S. Tensile Loading of Ropes of Single Wall Carbon Nanotubes and their Mechanical Properties. *Phys. Rev. Lett.* **2000,** *84* (24), 5552.

2. Saito, R.; Fujita, M.; Dresselhaus, G.; Dresselhaus, M. S. Electronic structure of chiral graphene tubules. *Applied Physics Letters* **1992,** *60* (18), 2204-2206.

3. Reich, S.; Thomsen, C. Chirality dependence of the density-of-states singularities in carbon nanotubes. *Phys. Rev. B* **2000,** *62* (7), 4273.

4. Saito, R.; Fujita, M.; Dresselhaus, G.; Dresselhaus, M. S. Electronic structure of graphene tubules based on C60. *Phys. Rev. B* **1992,** *46* (3), 1804.

5. Mintmire, J. W.; White, C. T. Universal Density of States for Carbon Nanotubes. *Phys. Rev. Lett.* **1998,** *81* (12), 2506.

6. Sze, S. M. 1981.
   Ref Type: Generic

7. Braun, E.; Neuringer, L. J. Trigonal Warping of the Energy Surfaces in Tellurium. *Phys. Rev. B* **1970,** *2* (6), 1553.

8. Saito, R.; Dresselhaus, G.; Dresselhaus, M. S. Trigonal warping effect of carbon nanotubes. *Phys. Rev. B* **2000,** *61* (4), 2981.

9. Kataura, H. Optical properties of single-wall carbon nanotubes. *Synth. Met.* **1999,** *103,* 2555-2558.

10. Dresselhaus, M. S.; Dresselhaus, G.; Jorio, A.; Souza, A. G.; Saito, R. Raman spectroscopy on isolated single wall carbon nanotubes. *Carbon* **2002,** *40,* 2043-2061.

11. Jorio, A. Structural (n, m) determination of isolated single-wall carbon nanotubes by resonant Raman scattering. *Phys. Rev. Lett.* **2001,** *86,* 1118-1121.

12. Bachilo, S. M.; Strano, M. S.; Kittrell, C.; Hauge, R. H.; Smalley, R. E.; Weisman, R. B. Structure-Assigned Optical Spectra of Single-Walled Carbon Nanotubes. *Science* **2002,** *298* (5602), 2361-2366.

13. Kataura, H.; Kumazawa, Y.; Maniwa, Y.; Umezu, I.; Suzuki, S.; Ohtsuka, Y.; Achiba, Y. Optical properties of single-wall carbon nanotubes. *Synthetic Metals* **1999,** *103* (1-3), 2555-2558.

14. Javey, A.; Guo, J.; Wang, Q.; Lundstrom, M.; Dai, H. Ballistic carbon nanotube field-effect transistors. *Nature* **2003,** *424* (6949), 654-657.

15. Javey, A.; Guo, J.; Paulsson, M.; Wang, Q.; Mann, D.; Lundstrom, M.; Dai, H. High-Field Quasiballistic Transport in Short Carbon Nanotubes. *Phys. Rev. Lett.* **2004,** *92* (10), 106804.

16. Zhang, Z.; Liang, X.; Wang, S.; Yao, K.; Hu, Y.; Zhu, Y.; Chen, Q.; Zhou, W.; Li, Y.; Yao, Y.; Zhang, J.; Peng, L. M. Doping-Free Fabrication of Carbon Nanotube Based Ballistic CMOS Devices and Circuits. *Nano Letters* **2007,** *7* (12), 3603-3607.

17. Bachtold, A. Aharonov-Bohm oscillations in carbon nanotubes. *Nature* **1999,** *397*, 673-675.

18. Choi, H. J.; Ihm, J.; Louie, S. G.; Cohen, M. L. Defects, quasibound states, and quantum conductance in metallic carbon nanotubes. *Phys. Rev. Lett.* **2000,** *84*, 2917-2920.

19. Bockrath, M. Resonant electron scattering by defects in single-walled carbon nanotubes. *Science* **2001,** *291*, 283-285.

20. Park, J. Y. Electron-phonon scattering in metallic single-walled carbon nanotubes. *Nano Lett.* **2004,** *4*, 517-520.

21. Lu, J. T.; Wang, J. S. Coupled electron and phonon transport in one-dimensional atomic junctions. *Physical Review B (Condensed Matter and Materials Physics)* **2007,** *76* (16), 165418-165419.

22. Steiner, M.; Freitag, M.; Perebeinos, V.; Tsang, J. C.; Small, J. P.; Kinoshita, M.; Yuan, D.; Liu, J.; Avouris, P. Phonon populations and electrical power dissipation in carbon nanotube transistors. *Nat Nano* **2009,** *advanced online publication*.

23. Park, J. Y.; Rosenblatt, S.; Yaish, Y.; Sazonova, V.; Ustunel, H.; Braig, S.; Arias, T. A.; Brouwer, P. W.; McEuen, P. L. ElectronΓêÆPhonon Scattering in Metallic Single-Walled Carbon Nanotubes. *Nano Letters* **2004,** *4* (3), 517-520.

24. Javey, A. High-field quasiballistic transport in short carbon nanotubes. *Phys. Rev. Lett.* **2004,** *92*, 106804.

25. Javey, A.; Qi, P.; Wang, Q.; Dai, H. Ten- to 50-nm-long quasi-ballistic carbon nanotube devices obtained without complex lithography. *Proceedings of the National Academy of Sciences of the United States of America* **2004,** *101* (37), 13408-13410.

26. Javey, A.; Guo, J.; Wang, Q.; Lundstrom, M.; Dai, H. Ballistic carbon nanotube field-effect transistors. *Nature* **2003,** *424* (6949), 654-657.

27. Tans, S.; Verschueren, A.; Dekker, C. Room-temperature transistor based on a single carbon nanotube. *Nature* **1998,** *393*, 49-52.

28. Martel, R.; Schmidt, T.; Shea, H. R.; Hertel, T.; Avouris, P. Single- and multi-wall carbon nanotube field-effect transistors. *Appl. Phys. Lett.* **1998,** *73*, 2447-2449.

29. Kim, W.; Javey, A.; Tu, R.; Cao, J.; Wang, Q.; Dai, H. Electrical contacts to carbon nanotubes down to 1 nm in diameter. *Applied Physics Letters* **2005,** *87* (17), 173101-173103.

30. Javey, A.; Guo, J.; Farmer, D. B.; Wang, Q.; Wang, D.; Gordon, R. G.; Lundstrom, M.; Dai, H. Carbon Nanotube Field-Effect Transistors with Integrated Ohmic Contacts and High-+¦ Gate Dielectrics. *Nano Letters* **2004,** *4* (3), 447-450.

31. Javey, A.; Wang, Q.; Ural, A.; Li, Y.; Dai, H. Carbon Nanotube Transistor Arrays for Multistage Complementary Logic and Ring Oscillators. *Nano Letters* **2002,** *2* (9), 929-932.

32. Chen, Z.; Appenzeller, J.; Lin, Y. M.; Sippel-Oakley, J.; Rinzler, A. G.; Tang, J.; Wind, S. J.; Solomon, P. M.; Avouris, P. An Integrated Logic Circuit Assembled on a Single Carbon Nanotube. *Science* **2006,** *311* (5768), 1735.

33. Martel, R.; Derycke, V.; Lavoie, C.; Appenzeller, J.; Chan, K. K.; Tersoff, J.; Avouris, P. Ambipolar Electrical Transport in Semiconducting Single-Wall Carbon Nanotubes. *Phys. Rev. Lett.* **2001,** *87* (25), 256805.

34. Back, J. H.; Kim, S.; Mohammadi, S.; Shim, M. Low-Frequency Noise in Ambipolar Carbon Nanotube Transistors. *Nano Letters* **2008,** *8* (4), 1090-1094.

35. Radosavljevic, M.; Heinze, S.; Tersoff, J.; Avouris, P. Drain voltage scaling in carbon nanotube transistors. *Applied Physics Letters* **2003,** *83* (12), 2435-2437.

36. Charlier, J. C.; Blase, X.; Roche, S. Electronic and transport properties of nanotubes. *Reviews of Modern Physics* **2007,** *79* (2), 677-56.

37. Bandow, S.; Asaka, S.; Saito, Y.; Rao, A. M.; Grigorian, L.; Richter, E.; Eklund, P. C. Effect of the Growth Temperature on the Diameter Distribution and Chirality of Single-Wall Carbon Nanotubes. *Phys. Rev. Lett.* **1998,** *80* (17), 3779.

38. Javey, A.; Kim, H.; Brink, M.; Wang, Q.; Ural, A.; Guo, J.; McIntyre, P.; McEuen, P.; Lundstrom, M.; Dai, H. High-[kappa] dielectrics for advanced carbon-nanotube transistors and logic gates. *Nat Mater* **2002,** *1* (4), 241-246.

39. Li, Y. Growth of single-walled carbon nanotubes from discrete catalytic nanoparticles of various sizes. *J. Phys. Chem.* **2001,** *105*, 11424-11431.

40. Krupke, R.; Hennrich, F.; Lohneysen, H.; Kappes, M. M. Separation of Metallic from Semiconducting Single-Walled Carbon Nanotubes. *Science* **2003,** *301* (5631), 344-347.

41. Hong, B. H.; Lee, J. Y.; Beetz, T.; Zhu, Y.; Kim, P.; Kim, K. S. Quasi-Continuous Growth of Ultralong Carbon Nanotube Arrays. *Journal of the American Chemical Society* **2005,** *127* (44), 15336-15337.

42. Jiao, L.; Xian, X.; Wu, Z.; Zhang, J.; Liu, Z. Selective Positioning and Integration of Individual Single-Walled Carbon Nanotubes. *Nano Letters* **2009,** *9* (1), 205-209.

43. Zheng, L. X. Ultralong single-wall carbon nanotubes. *Nature Mater.* **2004,** *3*, 673-676.

44. Yao, Y.; Li, Q.; Zhang, J.; Liu, R.; Jiao, L.; Zhu, Y. T.; Liu, Z. Temperature-mediated growth of single-walled carbon-nanotube intramolecular junctions. *Nat Mater* **2007,** *6* (4), 283-286.

45. Anderson, N.; Hartschuh, A.; Novotny, L. Chirality Changes in Carbon Nanotubes Studied with Near-Field Raman Spectroscopy. *Nano Letters* **2007,** *7* (3), 577-582.

46. Li, X.; Tu, X.; Zaric, S.; Welsher, K.; Seo, W. S.; Zhao, W.; Dai, H. Selective Synthesis Combined with Chemical Separation of Single-Walled Carbon Nanotubes for Chirality Selection. *Journal of the American Chemical Society* **2007,** *129* (51), 15770-15771.

47. Zhang, G.; Qi, P.; Wang, X.; Lu, Y.; Li, X.; Tu, R.; Bangsaruntip, S.; Mann, D.; Zhang, L.; Dai, H. Selective Etching of Metallic Carbon Nanotubes by Gas-Phase Reaction. *Science* **2006,** *314* (5801), 974-977.

48. Li, Y.; Mann, D.; Rolandi, M.; Kim, W.; Ural, A.; Hung, S.; Javey, A.; Cao, J.; Wang, D.; Yenilmez, E.; Wang, Q.; Gibbons, J. F.; Nishi, Y.; Dai, H. Preferential Growth of Semiconducting Single-Walled Carbon Nanotubes by a Plasma Enhanced CVD Method. *Nano Letters* **2004,** *4* (2), 317-321.

49. Bachtold, A.; Henny, M.; Terrier, C.; Strunk, C.; Schonenberger, C.; Salvetat, J. P.; Bonard, J. M.; Forro, L. Contacting carbon nanotubes selectively with low-ohmic contacts for four-probe electric measurements. *Applied Physics Letters* **1998,** *73* (2), 274-276.

50. Tersoff, J. Contact resistance of carbon nanotubes. *Applied Physics Letters* **1999,** *74* (15), 2122-2124.

51. Soh, H. T.; Quate, C. F.; Morpurgo, A. F.; Marcus, C. M.; Kong, J.; Dai, H. Integrated nanotube circuits: Controlled growth and ohmic contacting of single-walled carbon nanotubes. *Applied Physics Letters* **1999,** *75* (5), 627-629.

52. Park, N.; Hong, S. Electronic structure calculations of metal-nanotube contacts with or without oxygen adsorption. *Phys. Rev. B* **2005,** *72* (4), 045408.

53. Chen, Y. F.; Fuhrer, M. S. Tuning from Thermionic Emission to Ohmic Tunnel Contacts via Doping in Schottky-Barrier Nanotube Transistors. *Nano Letters* **2006,** *6* (9), 2158-2162.

54. Saito, T.; Yamada, T.; Fabris, D.; Kitsuki, H.; Wilhite, P.; Suzuki, M.; Yang, C. Y. Improved contact for thermal and electrical transport in carbon nanofiber interconnects. *Applied Physics Letters* **2008,** *93* (10), 102108-3.

55. Kim, H. S.; Jeon, E. K.; Kim, J. J.; So, H. M.; Chang, H.; Lee, J. O.; Park, N. Air-stable n-type operation of Gd-contacted carbon nanotube field effect transistors. *Applied Physics Letters* **2008,** *93* (12), 123106-3.

56. Lθonard, F.; Tersoff, J. Role of Fermi-Level Pinning in Nanotube Schottky Diodes. *Phys. Rev. Lett.* **2000,** *84* (20), 4693.

57. Heinze, S. Carbon nanotubes as Schottky barrier transistors. *Phys. Rev. Lett.* **2002,** *89*, 106801.

58. He, Y.; Zhang, J.; Hou, S.; Wang, Y.; Yu, Z. Schottky barrier formation at metal electrodes and semiconducting carbon nanotubes. *Applied Physics Letters* **2009,** *94* (9), 093107-3.

59. Manohara, H. M.; Wong, E. W.; Schlecht, E.; Hunt, B. D.; Siegel, P. H. Carbon Nanotube Schottky Diodes Using TiΓêÆSchottky and PtΓêÆOhmic Contacts for High Frequency Applications. *Nano Letters* **2005,** *5* (7), 1469-1474.

60. Yang, M. H.; Teo, K. B. K.; Milne, W. I.; Hasko, D. G. Carbon nanotube Schottky diode and directionally dependent field-effect transistor using asymmetrical contacts. *Applied Physics Letters* **2005,** *87* (25), 253116-3.

61. Appenzeller, J.; Radosavljevi-ç, M.; Knoch, J.; Avouris, P. Tunneling Versus Thermionic Emission in One-Dimensional Semiconductors. *Phys. Rev. Lett.* **2004,** *92* (4), 048301.

62. Lin, Y. M.; Appenzeller, J.; Avouris, P. Ambipolar-to-Unipolar Conversion of Carbon Nanotube Transistors by Gate Structure Engineering. *Nano Letters* **2004,** *4* (5), 947-950.

63. Derycke, V.; Martel, R.; Appenzeller, J.; Avouris, P. Controlling doping and carrier injection in carbon nanotube transistors. *Appl. Phys. Lett.* **2002,** *80*, 2773-2775.

64. Bachtold, A.; Hadley, P.; Nakanishi, T.; Dekker, C. Logic circuits with carbon nanotube transistors. *Science* **2001,** *294*, 1317-1320.

65. Tung, R. T. Recent advances in Schottky barrier concepts. *Materials Science and Engineering: R: Reports* **2001,** *35* (1-3), 1-138.

66. Berz, F. The Bethe condition for thermionic emission near an absorbing boundary. *Solid-State Electronics* **1985,** *28* (10), 1007-1013.

67. Baccarani, G. Current transport in Schottky-barrier diodes. *Journal of Applied Physics* **1976,** *47* (9), 4122-4126.

68. van Schilfgaarde, M.; Newman, N. Electronic structure of ideal metal/GaAs contacts. *Phys. Rev. Lett.* **1990,** *65* (21), 2728.

69. Peressi, M.; Binggeli, N.; Baldereschi, A. Band engineering at interfaces: theory and numerical experiments. *Journal of Physics D: Applied Physics* **1998,** *31* (11), 1273-1299.

70. Louie, S. G.; Chelikowsky, J. R.; Cohen, M. L. Ionicity and the theory of Schottky barriers. *Phys. Rev. B* **1977,** *15* (4), 2154.

71. Frenkel, J. On Pre-Breakdown Phenomena in Insulators and Electronic Semi-Conductors. *Phys. Rev.* **1938,** *54* (8), 647.

72. Kajiura, H.; Nandyala, A.; Coskun, U. C.; Bezryadin, A.; Shiraishi, M.; Ata, M. Electronic mean free path in as-produced and purified single-wall carbon nanotubes. *Applied Physics Letters* **2005,** *86* (12), 122106-3.

73. Purewal, M. S.; Hong, B. H.; Ravi, A.; Chandra, B.; Hone, J.; Kim, P. Scaling of Resistance and Electron Mean Free Path of Single-Walled Carbon Nanotubes. *Phys. Rev. Lett.* **2007,** *98* (18), 186808-4.

74. Yazyev, O. V.; Tavernelli, I.; Rothlisberger, U.; Helm, L. Early stages of radiation damage in graphite and carbon nanostructures: A first-principles molecular dynamics study. *Physical Review B (Condensed Matter and Materials Physics)* **2007,** *75* (11), 115418-5.

75. Krasheninnikov, A. V.; Nordlund, K.; Sirvio, M.; Salonen, E.; Keinonen, J. Formation of ion-irradiation-induced atomic-scale defects on walls of carbon nanotubes. *Phys. Rev. B* **2001,** *63*, 245405.

76. Smith, B. W.; Luzzi, D. E. Electron irradiation effects in single wall carbon nanotubes. *Journal of Applied Physics* **2001,** *90* (7), 3509-3515.

77. Gomez-Navarro, C.; Pablo, P. J. D.; Gomez-Herrero, J.; Biel, B.; Garcia-Vidal, F. J.; Rubio, A.; Flores, F. Tuning the conductance of single-walled carbon nanotubes by ion irradiation in the Anderson localization regime. *Nat Mater* **2005,** *4* (7), 534-539.

78. Marquardt, C. W.; Dehm, S.; Vijayaraghavan, A.; Blatt, S.; Hennrich, F.; Krupke, R. Reversible MetalΓêÆInsulator Transitions in Metallic Single-Walled Carbon Nanotubes. *Nano Letters* **2008,** *8* (9), 2767-2772.

79. Razouk, R. R.; Delfino, M.; Fulks, R. T.; Powell, R. A.; Yep, T. O. Oxide charges induced in thermal silicon dioxide by scanning electron and laser beam annealing. *Journal of Applied Physics* **1982,** *53* (1), 800-803.

80. Kim, W.; Javey, A.; Vermesh, O.; Wang, Q.; Li, Y.; Dai, H. Hysteresis Caused by Water Molecules in Carbon Nanotube Field-Effect Transistors. *Nano Letters* **2003,** *3* (2), 193-198.

81. Bleibaum, O.; B÷ttger, H.; Bryksin, V. V. Impact of the density of states on the dynamical hopping conductivity. *Phys. Rev. B* **2002,** *66* (10), 104203.

82. Grunewald, M.; Thomas, P. Simple calculation of the hopping conductivity for an exponential band tail. *physica status solidi (b)* **1979,** *94* (1), 125-133.

83. N.F.Mott, E. A. D. *Electronic Processes in Non-Crystalline Materials;* Clarendon Press: Oxford, 1979.

84. Appenzeller, J.; Martel, R.; Avouris, P.; Stahl, H.; Hunger, U. T.; Lengeler, B. Phase-coherent transport in ropes of single-wall carbon nanotubes. *Physical Review B (Condensed Matter and Materials Physics)* **2001,** *64* (12), 121404.

85. Fuhrer, M. S.; Cohen, M. L.; Zettl, A.; Crespi, V. Localization in single-walled carbon nanotubes. *Solid State Communications* **1998,** *109* (2), 105-109.

86. Pascual, J. I. Properties of metallic nanowires [mdash] from conductance quantization to localization. *Science* **1995,** *267*, 1793-1795.

87. Fuhrer, M. S.; Holmes, W.; Richards, P. L.; Delaney, P.; Louie, S. G.; Zettl, A. Nonlinear transport and localization in single-walled carbon nanotubes. *Synthetic Metals* **1999,** *103* (1-3), 2529-2532.

88. Ksenevich, V. K.; Odzaev, V. B.; Martunas, Z.; Seliuta, D.; Valusis, G.; Galibert, J.; Melnikov, A. A.; Wieck, A. D.; Novitski, D.; Kozlov, M. E.; Samuilov, V. A. Localization and nonlinear transport in single walled carbon nanotube fibers. *Journal of Applied Physics* **2008,** *104* (7), 073724-073727.

89. Nosho, Y.; Ohno, Y.; Kishimoto, S.; Mizutani, T. n-type carbon nanotube field-effect transistors fabricated by using Ca contact electrodes. *Applied Physics Letters* **2005,** *86* (7), 073105-3.

90. Bethe, H. A. *Theory of the Boundary Layer of Crystal Rectifiers;* MIT Radiation Laboratory: 1942.

91. Reich, S.; Thomsen, C.; Maultzsch, J. *Carbon Nanotubes: Basic Concepts and Physical Properties;* Wiley - VCH: New York, 2004.